



Cite this: DOI: 10.1039/c5nr01538c

## Photo-fluorescent and magnetic properties of iron oxide nanoparticles for biomedical applications

Donglu Shi,<sup>\*a,b</sup> M. E. Sadat,<sup>c</sup> Andrew W. Dunn<sup>a</sup> and David B. Mast<sup>c</sup>

Iron oxide exhibits fascinating physical properties especially in the nanometer range, not only from the standpoint of basic science, but also for a variety of engineering, particularly biomedical applications. For instance,  $\text{Fe}_3\text{O}_4$  behaves as superparamagnetic as the particle size is reduced to a few nanometers in the single-domain region depending on the type of the material. The superparamagnetism is an important property for biomedical applications such as magnetic hyperthermia therapy of cancer. In this review article, we report on some of the most recent experimental and theoretical studies on magnetic heating mechanisms under an alternating (AC) magnetic field. The heating mechanisms are interpreted based on Néel and Brownian relaxations, and hysteresis loss. We also report on the recently discovered photoluminescence of  $\text{Fe}_3\text{O}_4$  and explain the emission mechanisms in terms of the electronic band structures. Both optical and magnetic properties are correlated to the materials parameters of particle size, distribution, and physical confinement. By adjusting these parameters, both optical and magnetic properties are optimized. An important motivation to study iron oxide is due to its high potential in biomedical applications. Iron oxide nanoparticles can be used for MRI/optical multimodal imaging as well as the therapeutic mediator in cancer treatment. Both magnetic hyperthermia and photothermal effect has been utilized to kill cancer cells and inhibit tumor growth. Once the iron oxide nanoparticles are up taken by the tumor with sufficient concentration, greater localization provides enhanced effects over disseminated delivery while simultaneously requiring less therapeutic mass to elicit an equal response. Multi-modality provides highly beneficial co-localization. For magnetite ( $\text{Fe}_3\text{O}_4$ ) nanoparticles the co-localization of diagnostics and therapeutics is achieved through magnetic based imaging and local hyperthermia generation through magnetic field or photon application. Here,  $\text{Fe}_3\text{O}_4$  nanoparticles are shown to provide excellent conjugation bases for entrapment of therapeutic molecules, fluorescent agents, and targeting ligands; enhancement of solid tumor treatment is achieved through co-application of local hyperthermia with chemotherapeutic agents.

Received 9th March 2015,  
Accepted 30th March 2015

DOI: 10.1039/c5nr01538c  
[www.rsc.org/nanoscale](http://www.rsc.org/nanoscale)

### 1. Introduction

Clinical chemotherapeutic treatments often suffer from untargeted, systemic toxicities resulting in a multitude of unfavorable deleterious side effects. Localized hyperthermia through the application of radio frequencies, resistive heating, and hot water boluses has shown applicability as adjuvant treatment.<sup>1</sup> However an efficient method for highly localized, targeted delivery of therapeutic drugs is still needed. Magnetite ( $\text{Fe}_3\text{O}_4$ ) nanoparticles offer the convenient functionality of acting as a local heat source as well as providing a base for

conjugation of therapeutic molecules; thus offering highly tunable, customizable, multi-modal targeted therapeutics.<sup>2–7</sup> Near a hard radius of 10 nm, assuming a spherical shape, magnetite begins to exhibit superparamagnetism and is a product of this size regime coinciding the characteristic single domain crystal.<sup>8,9</sup> In this regime  $\text{Fe}_3\text{O}_4$  nanoparticles may induce localized environmental hyperthermia primarily through Néel and Brownian Relaxations of the magnetic domain when exposed to an alternating (AC) magnetic field, and heating from hysteresis losses appearing in larger particles.<sup>2,4,10–12</sup> Furthermore multi-modal imaging functionality is allowed through conjugation of fluorescent tags, as the  $\text{Fe}_3\text{O}_4$  nanoparticles possess innate magnetic traits allowing for imaging through nuclear magnetic resonance.<sup>13–16</sup> This fluorescence functionalization, as well as targeting, is readily achieved through surface conjugation of antibodies and fluorescent molecules through amide coupling.<sup>2,16–18</sup> Further functionalization may be obtained through silanol groups.<sup>19</sup>

<sup>a</sup>The Materials Science and Engineering Program, Department of Mechanical and Materials Engineering, College of Engineering and Applied Science, University of Cincinnati, Cincinnati, OH, USA. E-mail: [donglu.shi@uc.edu](mailto:donglu.shi@uc.edu)

<sup>b</sup>Shanghai East Hospital, The Institute for Biomedical Engineering and Nano Science, Tongji University School of Medicine, Shanghai, China

<sup>c</sup>Department of Physics, University of Cincinnati, Cincinnati, Ohio 45221, USA

Local hyperthermic induction through magnetic field application may not always be the preferred method. With the creation of small, portable alternating magnetic field generators patients need not be subjected to a large solenoids encompassing the full body. However for near surface tumors, especially in patients with magnetic field sensitive devices such as a pacemaker, an alternative induction method for local hyperthermia is preferred. Conveniently,  $\text{Fe}_3\text{O}_4$  nanoparticles have been recently observed to display a photothermal effect which allows for local environmental heating upon application of a near infrared (NIR) laser.<sup>20,21</sup> While this optically mediated hyperthermic response is limited by penetration depth into soft matter, it provides an efficacious treatment alternative when the alternating magnetic field is an un-preferred choice of therapy for certain patients. As localized hyperthermia from magnetic or optical induction may be combined with chemotherapeutic agents that are released in a spatially and temporally controlled manner,  $\text{Fe}_3\text{O}_4$  can be described as truly a multi-modal theranostic agent.<sup>22</sup>

## 2. Mechanism of magnetic hyperthermia

### 2.1 Different loss processes

In magnetic fluid hyperthermia, magnetic nanoparticles (MNPs) are usually exposed to the AC magnetic field. Heat dissipation from the magnetic nanoparticles generates a localized heat which can be used for possible application in cancer therapy. Three potential mechanisms are responsible for nanoparticles heating in AC field, namely: hysteresis loss, Néel relaxation, and Brownian relaxation. The dominant mechanism that are responsible for heating of nanoparticles in AC magnetic field depends upon the particle size, geometry, physical configuration, and viscosity. Therefore, it is important to understand the heat dissipation mechanism of different arrangement of particles for magnetic hyperthermia applications.

In general, hysteresis loss occurs in multidomain ferromagnetic particles when exposed to AC magnetic field. Due to the coupling of atomic spins with the lattice; electromagnetic energy is transferred to the lattice in the form heat, resulting in magnetically induced heating. The amount of heat generated during one cycle of the magnetic field is given by the area of the hysteresis loop. The hysteresis loop area ( $A$ ) is represented by:<sup>23</sup>

$$A = \int_{-H_{\max}}^{H_{\max}} \mu_0 M(H) dH \quad (2.1)$$

where,  $M(H)$  is the magnetization of the magnetic materials. The heating power or specific absorption rate (SAR) is defined as:  $SAR = Af$ , where  $f$  is the frequency of the applied magnetic field. Area of the hysteresis loop depends upon the magnetic nanoparticles size, anisotropy, frequency and amplitude of applied magnetic field.<sup>23</sup> The hysteresis loop of a magnetic

material can be described by three parameters, saturation magnetization ( $M_s$ ), remanent magnetization ( $M_r$ ) and coercivity ( $H_c$ ). Saturation magnetization is defined as the maximum magnetization achieved with increasing magnetic field. If the magnetic field is slowly reduced to zero, ferromagnetic materials retain some magnetization which is represented by remanent magnetization. To demagnetize the materials, a negative field is required, and the remanent field lost by the ferromagnetic material is called coercivity. All these three parameters have significance influence in heat dissipation by hysteresis.

As the particle size decreases, it is no longer able accommodate a domain wall, a condition characterized by a single-domain particle. A single domain particle possesses an energy barrier that impedes the moment alignment in the direction of field. Considerable energy is required for the entire domain to rotate under field. It was reported in a study of Heider *et al.*<sup>24</sup> that, in case of magnetite, the transition from multi-domain to single domain occurs at the particle diameter of 30 nm. Several experimental investigations on maghemite ( $\gamma\text{Fe}_2\text{O}_3$ ) and magnetite ( $\text{Fe}_3\text{O}_4$ ) nanoparticles have shown such transitions and particle size dependent coercivity.<sup>25</sup> As the size of the particles further reduces, for example to 18 nm of maghemite nanoparticles, a threshold is reached where particles' retentivity and coercivity goes to zero, a characteristic called "superparamagnetic." By analyzing several experimental data, Hergt *et al.*<sup>26</sup> reported a more general expression for coercivity ( $H_c$ ) as a function of particle size from multi- to single-domain region, which is represented as:

$$H_c(D) = H_M \left( \frac{D}{D_1} \right)^{-0.6} \left( 1 - e^{\left( -\frac{D}{D_1} \right)^5} \right) \quad (2.2)$$

where,  $H_M$  and  $D_1$  are the material specific parameter, for instance, a typical graph of coercivity as a function of particle size using eqn (2.2) is plotted in Fig. 3 of ref. 26, for the value of  $H_M = 32 \text{ kA m}^{-1}$  and  $D_1 = 15 \text{ nm}$  of magnetite.

When the particle sizes are in the superparamagnetic region, dissipation of heat in AC magnetic field usually occurs through either Néel or Brownian relaxation. In case of Néel relaxation, heat dissipation occurs when particles overcome an energy barrier ( $E$ ) in the presence of an alternating magnetic field ( $\mu_0 H_{\max}$ ), which is represented by:<sup>27</sup>

$$E(\theta, \varphi) = K_{\text{eff}} V \sin^2 \theta - \mu_0 H_{\max} M_s V \cos(\theta - \varphi) \quad (2.3)$$

where  $K_{\text{eff}}$  is the effective anisotropy constant,  $V$  is the volume of the particle,  $\theta$  is the angle between the anisotropy axis and magnetization, and  $\varphi$  is the angle between the applied magnetic field and anisotropy axis. At zero magnetic field, minimum energy of the particle occurs at, zero and  $\pi$ , which are the two equilibrium positions of the particle moment. However, as the temperature increases, thermal fluctuation is large enough to overcome the anisotropy barrier, which causes the magnetic moment of the particles to fluctuate rapidly in different anisotropic directions, resulting in zero net magneti-

zation for an assembly of superparamagnetic particles. This behavior of the particle is more analogous to the paramagnetic particles and can be described by an effective paramagnetic model. For a non-interacting system of superparamagnetic particles, the magnetization ( $M$ ) in an external magnetic field ( $H$ ) can be described by the Langevin function:<sup>28</sup>

$$M = M_s L(x) = M_s (\coth(x) - 1/x) \quad (2.4)$$

where,  $x = \frac{\mu_0 m H}{k_B T}$ , with  $m$  being the magnetic moment. The magnetic moment  $m$  can be extracted by fitting eqn (2.4) with experimental magnetization curve. Sadat *et al.*<sup>4</sup> reported such fittings for approximately 10 nm diameter superparamagnetic Fe<sub>3</sub>O<sub>4</sub> nanoparticles and found the magnetic moments are in the order of  $(2.3\text{--}6.4) \times 10^{-19}$  Am<sup>2</sup>, which is about 10<sup>5</sup> times higher than Bohr magneton. Thus superparamagnetic materials can be described as a single domain material with giant magnetic moment.

The characteristic time related to the thermal fluctuation of magnetization with different anisotropy axis is given by Arrhenius and first introduced by Néel in the following equation:<sup>29</sup>

$$\tau_N = \tau_0 \exp\left(\frac{K_{\text{eff}} V}{k_B T}\right), \quad (2.5)$$

where,  $\tau_0 \sim 10^{-9}\text{--}10^{-13}$  s.

In case of the Brownian relaxation, heating of the particles in liquid suspension occurs due to viscous drag between the particles and liquid, where the entire particle has a rotational movement with an applied AC magnetic field. The Brownian relaxation time is given by the following equation:<sup>30</sup>

$$\tau_B = \frac{3\eta V_H}{k_B T} \quad (2.6)$$

where  $\eta$  is the viscosity of the liquid and  $V_H$  is the hydrodynamic volume of the particle.

Generally, both Néel and Brownian relaxations can occur at the same time. The relaxation of the particle is characterized by the effective relaxation time  $\tau_{\text{eff}}$ , defined as:  $1/\tau_{\text{eff}} = 1/\tau_N + 1/\tau_B$ .

The time delay between the alignment time is defined as the measurement time  $\tau_m = 1/2\pi f$ , or the effective relaxation time which, at a given frequency, is responsible for dissipation of energy. Using  $\eta = 0.888$  mPa s<sup>-1</sup>, Sadat *et al.*<sup>4</sup> graphically represented an expression for Néel, Brownian, and effective relaxations as a function of particle diameter, as shown in Fig. 1(a) for different values of effective anisotropy constant ( $K_{\text{eff}}$ ), where the horizontal dashed line represents the measurement time (in this case 13.56 MHz) and vertical dashed line the inflection points where both Brownian and Néel relaxation processes are equally contributing to the energy dissipation.

From Fig. 1(a) it is clear that the critical particle diameter, where both Brownian and Néel relaxations contribute equally to hyperthermia heating, changes with anisotropy constant. Vallejo-Fernandez *et al.*<sup>31</sup> showed in a small field, at a certain critical particle diameter; hysteresis losses dominate over the susceptibility loss. This critical diameter is defined by:

$$D_p(0) = \left( \frac{6k_B T \ln(f\tau_0)}{\pi K_{\text{eff}}} \right)^{1/3} \quad (2.7)$$

where,  $\tau_0$  is assumed to be 10<sup>-9</sup> s,  $f$  is the frequency of the measurement. Neither Néel relaxation nor hysteresis loss contributes to the heating at this critical diameter. Most of the heating arises from stirring of the particles in the solutions. This critical diameter in an applied field ( $H$ ) is defined as:

$$D_p(H) = \left[ 1 - \frac{HM_s}{0.9K_{\text{eff}}} \right]^{-2/3} D_p(0) \quad (2.8)$$

Fig. 1(b), shows the contribution of heating due to a different mechanism for an effective anisotropy value of  $K_{\text{eff}} = 30$  KJ m<sup>-3</sup> and at an applied field of 250 Oe and 111.5 kHz. It was shown that the critical diameter below which Néel relaxation or susceptibility loss dominates is 13.5 nm and heating due to stirring takes place above 19.4 nm. Hysteresis loss occurs only in the region between  $D_p(0) < D < D_p(H)$ . This analysis leads to a conclusion that for a highly polydisperse

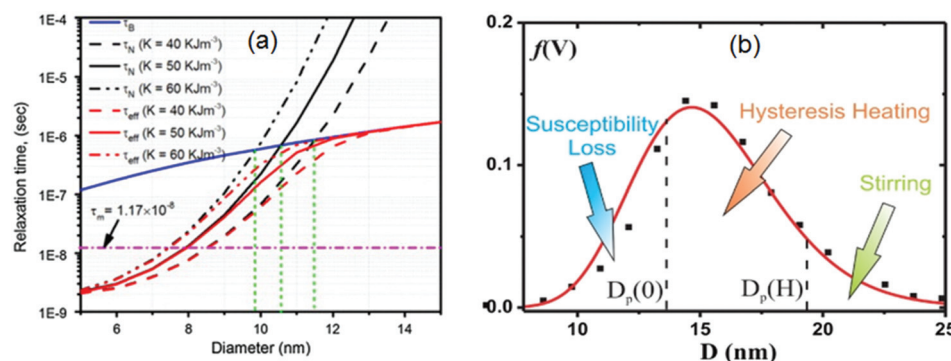


Fig. 1 (a) Graphical representation of Brownian, Néel and effective relaxation times as a function of particle diameter for different values of anisotropy constant ( $K$ )<sup>4</sup> and (b) representation of heating due to Néel and Brownian relaxations, and hysteresis loss.<sup>31</sup> [Part (a) of the figure is reproduced with permission from Elsevier © 2014 Elsevier B.V. and part (b) is reproduced with permission from IOP Publishing © 2013 IOP Publishing. All rights reserved].

sample all three mechanisms of heating can be effective. A more detailed analysis and review of literature about effect of size and size distribution on magnetic hyperthermia heating will be discussed in section 2.3.

## 2.2 Effects of field and frequency on heating behavior

In the previous section, heating of MNPs in alternating magnetic field is described in terms of Brownian and Néel relaxations and hysteresis loss. For clinical applications, the appropriate dosage of MNPs in malignant tissue needs to generate sufficient heat, which is characterized by Specific Absorption Rate (SAR). According to Rosensweig, SAR depends on the amplitude ( $H$ ) and frequency ( $f$ ) of the alternating magnetic field by the following equation:<sup>30</sup>

$$\text{SAR} = \frac{\mu_0 H^2 2\pi^2 f^2 \chi_o \tau_{\text{eff}}}{1 + (2\pi f \tau_{\text{eff}})^2} \quad (2.9)$$

SAR also depends on the local properties such as viscosity and heat capacity of the carrier liquid or surrounding tissue. Thus the frequency dependence of Brownian or Néel relaxation loss needs to be investigated. The susceptibility of the magnetic fluid in AC field can be written in terms of real and imaginary components by the equation:

$$\chi(\omega) = \chi'(\omega) - i\chi''(\omega) \quad (2.10)$$

Debye has successfully demonstrated that complex susceptibility is frequency dependent, also considering the particle size distribution, the equation for complex susceptibility can be written as:<sup>32</sup>

$$\chi(\omega) - \chi_\infty = (\chi_o - \chi_\infty) \int_0^\infty \left[ \frac{1}{1 + \omega^2 \tau_{\text{eff}}^2} - \frac{i\omega\tau}{1 + \omega^2 \tau_{\text{eff}}^2} \right] f(\tau) d\tau \quad (2.11)$$

where  $\chi_o$  is the susceptibility at low field,  $\chi_\infty$  indicates the susceptibility at very high frequency and  $\tau_{\text{eff}} = \frac{1}{2\pi f_{\text{max}}}$ ,  $f_{\text{max}}$  is the frequency where maximum of imaginary susceptibility appears. Using toroidal technique, Fannin *et al.* reported on the complex susceptibility in the frequency range of 5 Hz–

13 MHz for 10 nm size  $\text{Fe}_3\text{O}_4$  nanoparticles dispersed in different carrier liquids, such as water and kerosene.<sup>33</sup> It was found that the water-based  $\text{Fe}_3\text{O}_4$  nanoparticles showed a pronounced and broad peak on the imaginary susceptibility spectra at 5.5 kHz [Fig. 2a], which corresponds to the particle hydrodynamic diameter of 27 nm. A peak at 18 kHz and 0.9 MHz was found for the kerosene-based ferrofluid [Fig. 2b], corresponding to the particle hydrodynamic diameter of 18 nm and 5 nm respectively. Considering the viscosities of two carrier liquids, the peak in the low frequency region can be attributed to Brownian relaxation, whereas that in the high frequency region to Néel relaxation. The difference in peak positions between the two samples was due to considerable agglomeration in water-based ferrofluid with a larger hydrodynamic diameter compared to the kerosene-based fluid. Using the same technique as described in Fannin's article, Hanson *et al.*<sup>34</sup> showed the maximum of imaginary part occurring at 8.5 MHz for the kerosene-based ferrofluid. But dilution shifted the peak position to higher frequencies, indicating stronger dipolar interactions in the more concentrated samples. Their results concluded Néel relaxation a dominant mechanism in the MHz range.

Chen *et al.*<sup>35</sup> investigated the complex AC susceptibility of 10 nm- $\text{Fe}_3\text{O}_4$  nanoparticles embedded in the polystyrene matrix (PS/ $\text{Fe}_3\text{O}_4$ ). The hydrodynamic size distributions of the NPs are in the region between 60 nm to 200 nm. The low field AC susceptibility measurement of these samples shows a broad peak at ~300 Hz, which fits quite well with the Brownian relaxation process.

In addition to Brownian and Néel relaxations, ferromagnetic resonance can also be observed at microwave frequencies. The observation of ferromagnetic resonance at approximately ~1.2 GHz was reported in several studies.<sup>36–38</sup> Microwave absorption may not be suitable for magnetic hyperthermia therapy, but useful for microwave – based device applications, for instance, the microwave – assisted protein digestions and magnetic resonance imaging contrast agent.<sup>39,40</sup> These studies have shown that the absorption properties of MNPs in AC field can be tuned by changing the hydrodynamic diameter, anisotropy constant, and the geometry of the particles.

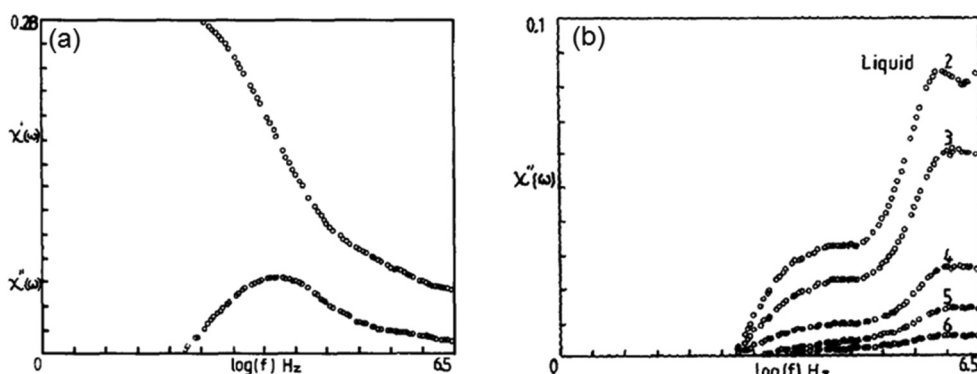


Fig. 2 Complex susceptibility of (a) water based ferrofluid (EMG 607) and (b) kerosene based ferrofluid (EMG 905) with decreasing concentration as a function of log frequency.<sup>33</sup> [Part (a, b) is reproduced with permission from Elsevier © 1988 Elsevier B.V. All rights reserved].

### 2.3 Effects of size, size distribution, and shapes of nanoparticles

For the diameter of a MNP in the range between  $10 \text{ nm} < r < 60 \text{ nm}$ , the magnetization of a single magnetic domain (SD) can assume two “easy” crystallographic directions separated by an anisotropic energy barrier. Due to its small size, the magnetization direction becomes thermally randomized above a blocking temperature ( $T_B$ ). Below  $T_B$ , particles display single domain behavior, leading to what is termed the “superparamagnetic” state, where the system retentivity and coercivity goes to zero. The blocking temperature is determined by the anisotropy constant (energy barrier) of the material and volume of the particles. In magnetic hyperthermia, under an alternating magnetic field, energy is dissipated, in form of heat, from the magnetic nanoparticles either due to relaxation or hysteresis loss. When the local heat generated *via* cell-targeted uptake in the tumor region reaches therapeutic threshold, cancer cells can be effectively killed. In practice, for efficient heating ability, MNPs need to absorb sufficient amount of magnetic energy. Iron oxide nanoparticles exhibit different heating properties depending upon the particle size, size distribution, shape, and physical arrangement.

Carrey *et al.*<sup>23</sup> proposed a model correlating the magnetic nanoparticles size or volume to heat dissipation for optimization of magnetic hyperthermia applications. According to their study, hysteresis losses are the main mechanisms responsible for heating by MNPs of any sizes. Therefore it is required to calculate the area of hysteresis loop and estimate the

amount of heat dissipation from MNPs. Their model is based upon three important theories on hysteresis losses, which are: equilibrium functions,<sup>41</sup> linear response theory (LRT) based on Néel–Brownian relaxation processes, and the Stoner–Wohlfarth model (SWM). Fig. 3 shows a schematic illustration of the hysteresis loss as a function of nanoparticle volume.

To define heat dissipation of different volume of nanoparticles, two dimensionless parameters are assumed, which are described by the equation:

$$\kappa = \frac{k_B T}{k_{\text{eff}} V} \ln \left( \frac{k_B T}{4\mu_0 H_{\max} M_s V f \tau_0} \right) \quad (2.12)$$

and,

$$\xi = \frac{\mu_0 H_{\max} M_s V}{k_B T} \quad (2.13)$$

where,  $k_B$  is the Boltzmann constant,  $T$  is the absolute temperature,  $K_{\text{eff}}$  is the effective uniaxial magnetic anisotropy constant,  $V$  is the particles volume,  $\mu_0 H_{\max}$  is the magnetic field, and  $f$  is the frequency. As can be seen from the figure, for small particles in the superparamagnetic regime, where  $\kappa > 1.6$ , the magnetization curve is completely reversible and no hysteresis loss can be observed, leading to minimal heating. The magnetization behavior of this type of particles can be described by equilibrium functions and LRT. The region where LRT is valid and decreases with increasing volume is labeled by (1) in Fig. 3. The superparamagnetic to ferromagnetic transition is represented as  $\omega \tau_N = 1$ ; above  $\omega \tau_N > 1$ , MNPs are in

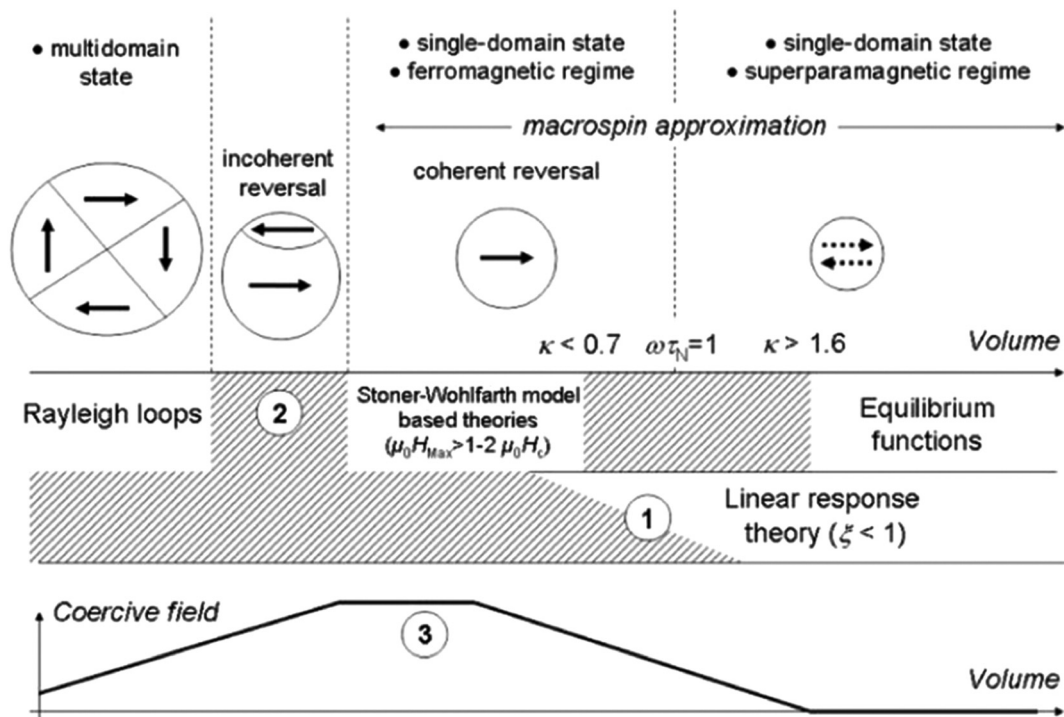


Fig. 3 Schematic representation of the evolution of the magnetic properties of MNPs as a function of their volume and of the models suitable to describe them.<sup>23</sup> [Fig. 3 is reproduced with permission from AIP publishing © AIP publishing. All rights reserved.]

the ferromagnetic regime and hysteresis loop progressively increases with increasing nanoparticles volume. Hysteresis loop in this region can be described by the SWM model. As the size increases further, incoherent reversal mode starts to grow and coercive field decreases. As predicted by SWM, the hysteresis loss becomes insignificant. The region where incoherent reversal mode occurs is designated as label (2) in Fig. 3. A plateau in the coercive field as a function of volume is labeled as (3) in this figure. For very large sizes, the particles contain multiple magnetic domains separated by domain walls and their hysteresis loops in this regions can be described by the Rayleigh loops.

For an ideal monodisperse sample, the magnetic properties can be described by above theories. Under real conditions, however, the effect of polydispersity is responsible for magnetic heating. Heating is influenced by several mechanisms including superparamagnetism and ferromagnetism. Dormann *et al.*<sup>42</sup> reported that, for a non uniform distribution of particle sizes, the size distributions can be well described by a log normal distribution:

$$f(d) = \frac{1}{\sqrt{2\pi}\sigma d} \exp\left[-\left(\ln \frac{d}{d_c}\right)^2 \frac{2}{2\sigma^2}\right] \quad (2.14)$$

where,  $d_c$  is the mean particle diameter and  $\sigma$  is the standard deviation.

Effects of size and size distributions on hysteresis losses of MNPs in magnetic hyperthermia were investigated by Hergt *et al.*<sup>26</sup> According to their analysis, an enhancement of specific loss power (SLP) of the iron oxide nanoparticle samples can be possible by preparing narrow size distribution with an average diameter in the range of single domain range which exhibits maximum coercive field. The experimental investigation was carried out by Fortin *et al.* on the effects of size and size distribution on heating behavior of the maghemite nanoparticles with size ranging from 5.3 nm to 16.5 nm in alternating magnetic field.<sup>43</sup> It was found that at a frequency of 700 kHz and field amplitude of 24.8 KA m<sup>-1</sup>, specific loss power (SLP) can be significantly increased from 4 W g<sup>-1</sup> to 1650 W g<sup>-1</sup> which is almost 3 orders of magnitudes higher when the size was increased from 5.3 nm to 16.5 nm. They found heating to be mainly caused by Néel relaxation. In addition to the study on size dependence, they also found a marked decrease in SLP when polydispersity increased from 0 to 0.4. A similar investigation was carried out by Gonzales-Weimuller *et al.* with the same conclusions.<sup>44</sup>

Despite these extensive investigations, the main mechanism responsible for hyperthermia heating is still not well understood, as the hysteresis loss was not included in the study of Fortin *et al.* Vallejo-Fernandez *et al.*<sup>31</sup> investigated the magnetic heating behavior of magnetite/maghemite nanoparticles at 115 kHz magnetic field and found insignificant Néel relaxation. They therefore concluded that the hysteresis loss due to stirring is mainly responsible for heating for particle

size range of 10–15 nm. Interestingly, their findings show that heating was 43% lower when the particles were dispersed in wax compared to in liquid solvent, which simulates to an *in vivo* environment.

To classify different regions, size dependent heating mechanism of 5–18 nm iron oxide nanoparticles was investigated by Bakogiannis *et al.*<sup>45</sup> They correlated coercivity, saturation magnetization, and SLP to the particle sizes. Superparamagnetic region was represented by the particle size of 10 nm; and its transition to the ferromagnetic region was denoted as 10–13 nm. The ferromagnetic region was characterized by the particle diameter above 13 nm. They demonstrated Néel relaxation to be mostly responsible for heating by particles of 10 nm, while hysteresis heating dominates for particle size above 10 nm, as the most efficient process.

In addition to size and size distribution study, effects of nanoparticle shapes,<sup>46,47</sup> surrounding environment or viscosity,<sup>48</sup> and anisotropy<sup>49,50</sup> on hyperthermia heating in AC magnetic field were also investigated previously by many researchers. The key issue has been the particle clustering mechanism in magnetic ferrofluids, as it may change the global magnetic behavior due to dipolar interactions between particles. The effects of magnetic interactions on hyperthermia heating is discussed in the following section.

## 2.4 Effects of magnetic interactions

The fundamental parameters that influence the heating ability of the nanoparticles in AC field include frequency ( $f$ ), amplitude of the magnetic field ( $H$ ), particle size and size distributions, and geometry of the particles. Magnetic dipole interactions underline several important physical behaviors such as hyperthermia heating. In particular, in a complex biological system, nanoparticles are inhomogeneously distributed and intercellular clustering of nanoparticles into endosomes or different sub cellular compartment<sup>51,52</sup> may lead to a substantially different heating behavior from the *in vitro* observation. Clinically, a consistency is required between *in vitro* and *in vivo* settings before the nanoparticle – mediated magnetic hyperthermia is implemented for therapy.

The role of dipole interactions on hyperthermia can be experimentally investigated by changing the interparticle separation and physical confinement of the nanoparticles in a nonmagnetic matrix. In a study by Sadat *et al.*<sup>4,5</sup> two different nanoparticle systems were established. One composed of ~10 nm Fe<sub>3</sub>O<sub>4</sub> nanoparticles coated with poly(acrylic) acid (PAA/Fe<sub>3</sub>O<sub>4</sub>) and uniformly dispersed in water, while the other consists of the similar Fe<sub>3</sub>O<sub>4</sub> nanoparticles embedded in a polystyrene matrix of spherical shape with a diameter of ~100 nm (denoted as PS/Fe<sub>3</sub>O<sub>4</sub>). It was found in their study that these nanoparticle systems behaved differently when exposed to an applied AC field of 13.56 MHz and 4500 A m<sup>-1</sup>. The specific absorption rate (SAR) of PS/Fe<sub>3</sub>O<sub>4</sub> was found to be 37% lower than that of PAA/Fe<sub>3</sub>O<sub>4</sub>. This difference is explained by the confined particles in the polystyrene matrix (PS/Fe<sub>3</sub>O<sub>4</sub>) having stronger dipole interactions due to smaller interparticle separations. When physically confined in the polystyrene

matrix with short interparticle distances, the magnetic moment is impeded by strong dipole interactions therefore largely reducing the Néel relaxation effect. The heating is mainly caused by hysteresis losses. It was also found that SAR progressively decreased with increasing volume fractions. A similar observation was also reported by Urtizberea *et al.*<sup>53</sup> Their observation showed that, at frequency of 109 kHz with field amplitude of 3000 A m<sup>-1</sup>, SAR of the 11.6 nm maghemite nanoparticles was increased by 100% as the ferrofluid concentration decreased by 4 fold. Both observations suggested stronger dipole interactions by either increasing concentration or spatial confinement of the nanoparticles. Urtizberea *et al.* described this behavior by using several different theoretical models,<sup>53–56</sup> among which the Berkov and Gorn (BG) model<sup>57</sup> appeared to be more plausible on the correlation between SAR and the magnetic properties of the specific samples. Furthermore, Martinez Boubeta, *et al.*<sup>58</sup> and Piñeiro-Redondo *et al.*<sup>59</sup> made similar conclusions based on the dipole interactions.

The numerical simulations of dipole-dipole interactions on hyperthermia heating were performed by several researchers.<sup>60–63</sup> Haase *et al.*<sup>60</sup> analyzed the hyperthermia heating abilities of 15 nm particles with a anisotropy constant of

$K = 10 \text{ kJ m}^{-3}$  and saturation magnetization of  $M_s = 800 \text{ KA m}^{-1}$ , by fast Fourier transformation method.<sup>64</sup> Their simulations showed progressive decreasing of the hysteresis loop area with increasing volume fractions due to dipole interactions [Fig. 4a]. Simulation of frequency and damping factor indicated small influence on hysteresis loss. The results on the qualitative behaviors are shown in Fig. 4a and b. The influence of hyperthermia of 75 nm ferromagnetic Fe particles with MgO coating under AC field was investigated by Serantes *et al.*<sup>61</sup> by using Metropolis algorithm with local dynamics.<sup>63</sup> They found the decrease in hyperthermia to be associated with the dipole interactions.

It can be concluded that the heat dissipation mechanism is closely associated with dipole-dipole interactions in AC magnetic field for both superparamagnetic and ferromagnetic nanoparticles. In general, superparamagnetic particles dissipate heat by Néel and Brown relaxations and follow the classical Langevin behavior, *i.e.* reversible magnetization curve with zero retentivity and coercivity. But at high concentrations, they seem to be deviated from the Langevin behavior and dipole interactions play a major role in changing the anisotropy and magnetic behavior of these particles. Singh *et al.*<sup>65</sup> investigated the heat dissipation mechanism of 10 nm superparamagnetic

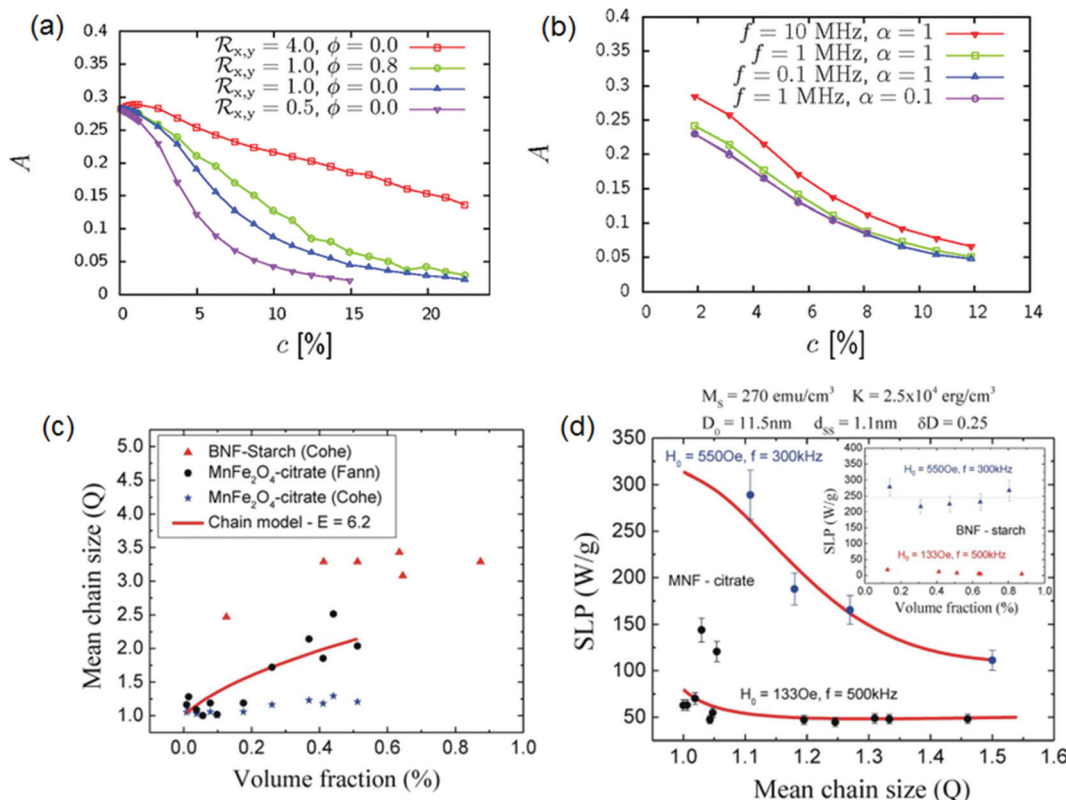


**Fig. 4** Hysteresis area ( $A$ ) as a function of particle concentration for (a) different sample shape ( $\mathcal{R}_{x,y}$ ) and size distributions ( $\phi$ ), (b) different frequency ( $f$ ) and damping factor ( $\alpha$ ),<sup>60</sup> (c) mean chain size as a function of particle volume fraction for MNF (coherent and fanning) and BNF (coherent) samples, where the solid line represents the best fit of the MNF fanning data using the chain model and (d) SLP as function of mean chain size for the MNF sample at different experimental conditions, where solid lines represents the fitting of SLP using theoretical model described in ref. 51. The inset shows the data for the BNF-starch sample.<sup>51</sup> [Part (a, b) of the figure is reproduced with permission from American Physical Society © 2012 American Physical Society and part (c, d) is reproduced with permission from Nature © 2013 Nature Publishing Group. All rights reserved.]

magnetite nanoparticles of various suspension concentrations. It was found that when particles were sufficient in number in the suspensions, they created a dipolar field resulting in enhanced heat dissipation. In support of their analysis, experimental results by Gudoshnikov *et al.*<sup>66</sup> and Fortin *et al.*<sup>67</sup> showed distinctive heat dissipations, *via* magnetic hysteresis losses, from the magnetite nanoparticles in glue and maghemite nanoparticles in water suspension respectively.

Recent theoretical and experimental studies show that particles are more prone to chain formation in AC magnetic field. Luis C. Branquinho *et al.*<sup>51</sup> showed that SAR of ferrite-based nanoparticles decreases with increasing volume fractions due to formation of chains. As can be seen from Fig. 4c, mean chain size increases with increasing volume fraction. As can also be seen in Fig. 4d, SLP decreases as mean chain size increases. They demonstrated optimum experimental conditions including the chain size and the particle size which all significantly affected the heating ability of the MNPs. The formation of dimers and agglomeration of particles at various volume fractions was also reported by Castro *et al.*<sup>68</sup> using the Monte Carlo simulations of ferrofluids.<sup>69</sup> Despite of extensive research on magnetic nanoparticles, further studies are needed on the development of high level computational methods for complex biological systems and magnetic hyperthermia therapy.<sup>50</sup>

### 3. Synthesis

Magnetite nanoparticles of various sizes, surfaces, and spatial confinements have been successfully synthesized by a myriad of procedures including: facile polyol, co-precipitation, hydrothermal decomposition, and micro/miniemulsion. Polyol procedures involve nanoparticle formation in a pure phase glycol or a polyglycol/glycol mixture. This allows for high temperature synthesis of a monodisperse size. Furthermore, the polyglycol(s) employed are observed to surface adsorb, enhancing colloidal stability. Such procedures have been accomplished by Hu *et al.*<sup>15</sup> and Dai *et al.*<sup>16</sup> using the iron salt of iron(III) tri(acetylacetone) dissolved in a combination of poly(ethylene glycol) bis(carboxymethyl) ether and triethylene glycol. Upon dissolution of the iron salt precursor at 100 °C, the temperature of the reaction medium was raised to 210 °C for 2 h followed by a refluxing period of one hour at 287 °C producing magnetite nanoparticles, surface – functionalized with adsorbed poly(ethylene glycol) bis(carboxymethyl) ether and triethylene glycol possessing an average hydrodynamic diameter of 12 nm throughout a wide pH range.

A similar approach was used to successfully increase the size of previously synthesized magnetite nanoparticles by the addition of the preformed nanoparticles to the reaction medium to act as surface catalytic sites. Completion of the polyol synthesis using iron(III) tri(acetylacetone) in phenyl ether, 1,2-hexadecanediol, oleic acid, and oleylamine with mixed preformed Fe<sub>3</sub>O<sub>4</sub> nanoparticles of 4 nm size yielded 16 nm diameter particles highly monodisperse in size.<sup>8</sup> This

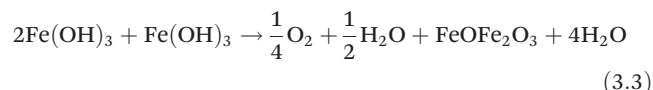
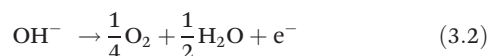
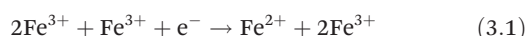
method was also successfully used in the condensation of silicon dioxide shells onto Fe<sub>3</sub>O<sub>4</sub> nanoparticle to create highly monodisperse core shell SiO<sub>2</sub>–Fe<sub>3</sub>O<sub>4</sub> constructs.<sup>70</sup>

#### 3.1 Co-precipitation

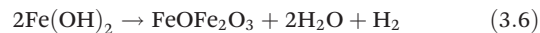
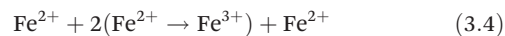
Co-precipitation relies on the precipitation of and subsequent reduction of iron(III) oxyhydroxide (FeO·OH) and iron(II) hydroxide [Fe(OH)<sub>2</sub>] into magnetite. Hydrothermal decomposition takes a similar approach through the formation of the FeO·OH and Fe(OH)<sub>2</sub> compounds before forming crystalline magnetite. However a fundamental difference is the pH at which the two synthesis methods operate. Thermal decomposition is completed without the necessity of the establishment of a basic environment to achieve the crystalline magnetite whereas co-precipitation requires excess hydroxide for the establishment of a basic solution. During these synthesis procedures, the chemical environment may provide necessary constituents for co-condensation of coating agents such as polymeric species, silicon dioxide layers, and the surface adsorption of colloidal stabilization agents. Under anaerobic conditions.

Under basic conditions, iron in the (2+) or (3+) valence state spontaneously forms iron oxyhydroxide which may be further converted into magnetite nanoparticles through Fe<sup>3+</sup> reduction, eqn (3.1)–(3.3), Fe<sup>2+</sup> oxidation (Schikorr reaction, eqn (3.4)–(3.6), or through co-precipitation of Fe<sup>3+</sup>/Fe<sup>2+</sup> detailed by eqn (3.7) and (3.8).<sup>71–73</sup> Co-precipitation of Fe<sup>3+</sup>/Fe<sup>2+</sup> in basic conditions is highly dependent on both pH of the reaction medium and the stoichiometric ratio of the added Fe<sup>3+</sup>/Fe<sup>2+</sup> iron ions with a preferred pH near 11 and a Fe<sup>3+</sup>/Fe<sup>2+</sup> ration of 2 : 1.<sup>73,74</sup>

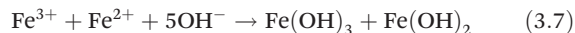
##### By Fe<sup>3+</sup> reduction



##### Schikorr reaction



##### By Fe<sup>3+</sup>/Fe<sup>2+</sup> co-precipitation



#### 3.2 Micro/nanoemulsion

Emulsion methods rely on the utilization of immiscible solvents. Precursors are generally dissolved in a high or low

dielectric solvent depending on the solubility of the precursors. Ultrasonication of synthesis precursors can assist in creating a homogeneous environment prior to creation of the micro/nanoemulsion system which may contain metal salts, coating agents, therapeutic, and diagnostic reagents. Establishment of the emulsion systems is completed through addition of a dispersant with a drastically different dielectric constant than the solvent used to solubilize the precursors/theranostic agents combined with vigorous stirring or through membrane emulsification.<sup>75</sup> A water-in-oil system (W/O) is established in which water or a similar solvent, solubilizing the carrier molecules of interest, forms micro/nanobeads dispersed in a low dielectric solvent such as *N,N*-dimethylformamide, acrylonitrile, and acetone, the ‘oil’ phase. Establishment of an oil-in-water (O/W) system is comparative to the W/O system albeit the micro/nanobeads are suspended of the ‘oil’ phase and dispersed in the ‘water’ phase. A related method to micro/nanoemulsion is membrane emulsion which utilizes highly tunable synthetic membranes such as polyether-sulfone and cellulose acetate to generate the micro/nano beads through membrane diffusion in which synthesis reactions occur, rather than through mechanical stirring or sonication.<sup>76</sup>

Successful creation of a functionalized polystyrene entrapped multi-core magnetite nanosphere was completed through a modified method described by Hong Xu *et al.*<sup>75</sup> Initially  $\text{Fe}_3\text{O}_4$  nanoparticles were generated by co-precipitation through the addition of concentrated ammonium hydroxide to a mixture of  $\text{Fe}^{2+}/\text{Fe}^{3+}$  iron ions in an aqueous environment. An important component of the nanoemulsion method is the establishment of separate phases with the capping agent and metallic oxide core solubilized in the same phase. Bead emulsions of polystyrene monomers may be easily generated by ultrasonication or membrane sonication, but exist in the “oil” phase, whereas synthesized  $\text{Fe}_3\text{O}_4$  nanoparticles possesses an innate hydrophilicity. An alteration to the surface properties of the magnetite nanoparticles is required to create the polystyrene entrapped multi-nuclei  $\text{Fe}_3\text{O}_4$  nanospheres. Without the phase solubility modification of  $\text{Fe}_3\text{O}_4$  nanoparticles,

micro/nanoemulsions of polystyrene monomers will polymerize to become polystyrene spheres void of  $\text{Fe}_3\text{O}_4$  nanoparticles.

A convenient solubility phase modifier, and the solubility modifier used here to generate the nanospheres in Fig. 5a, is oleic acid (OA). With the inclusion of OA with the  $\text{Fe}_3\text{O}_4$  nanoparticles dispersed in an aqueous environment, the solubility phase of the nanoparticles is altered to low dielectric constant solvents. As the OA is heated above its melting temperature and is incorporated into the aqueous system in liquid phase, the carboxylic acid functional groups on the end of the OA chain chemiadsorb onto the  $\text{Fe}_3\text{O}_4$  nanoparticle surface.<sup>77</sup> The highly saturated alkane chains then freely populate the nanoparticle surface effectively encompassing the nanoparticle in a sheath of hydrophobic alkane chains and thereby switching the solubility phase from a high to a low dielectric solvent. As a direct result of this important step, metal oxides may then be encased in polymeric species which solubilize in the “oil” phase. Following this addition of OA the newly coated  $\text{Fe}_3\text{O}_4$  nanoparticles then stabilized in an aqueous phase through the addition of sodium dodecyl sulfate (SDS) as a surfactant. The formed nanoemulsion of SDS-OA- $\text{Fe}_3\text{O}_4$  was then mixed with a microemulsion of polystyrene monomers, prepared through membrane emulsion, and the double emulsion system was reacted at 80 °C for 20 hours, forming the polystyrene encapsulated multi-nuclei nanospheres shown in Fig. 5a (PS/ $\text{Fe}_3\text{O}_4$ ).

Incorporation of poly(ethylene oxide) (PEO) onto the surface of the PS/ $\text{Fe}_3\text{O}_4$  nanospheres has allowed for covalent linkage of quantum dots through carbodiimide coupling and allows for a multitude of functionalization possibilities as this linkage technique is largely universal and easily conducted.<sup>2</sup> Quantum dots were able to be conjugated onto the surface of the PS/ $\text{Fe}_3\text{O}_4$  through a covalent amide bond. Primary amine functionalized PEO conjugated quantum dots under the trade name Qdot® 800 ITK™ Amino (PEG) Quantum Dots were used in conjunction with the common carbodiimide coupling agent 1-ethyl-3-(3-dimethylaminopropyl) carbodiimide-HCL (EDC). Polysorbate was used in place of SDS as the surfactant, allowing for incorporation of polysorbate units into the surface of

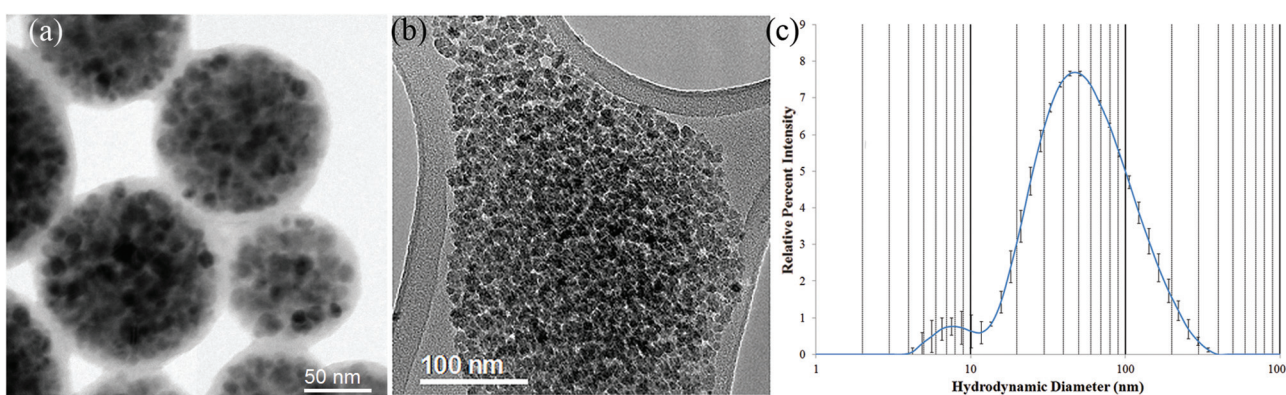


Fig. 5 (a) TEM image of PS/ $\text{Fe}_3\text{O}_4$  microspheres showing the amorphous coating entrapping multiple  $\text{Fe}_3\text{O}_4$  nuclei. (b) TEM image of PAA/ $\text{Fe}_3\text{O}_4$  (c) cumulant size distribution of PAA/ $\text{Fe}_3\text{O}_4$  showing a maximum near 50 nm.

the polymerized PS sphere. Necessary carboxylic acid groups for carbodiimide coupling were then generated through cleavage and auto-oxidation of the PEO side chains of the incorporated polysorbate. Tail vein injected quantum dot functionalized PS/Fe<sub>3</sub>O<sub>4</sub> were easily tracked using fluorescent imaging of nude mice. Systemic accumulation is shown in Fig. 9.

### 3.3 Decomposition

Decomposition provides a convenient method of nanoparticle formation from iron and other metal precursors. Relying on thermal induction of precursor decomposition, reaction vessels may be heated at an elevated temperature for an extended period of time without the need to vessel observation and system adjustment. Fe<sub>3</sub>O<sub>4</sub> nanoparticles recently used in novel biological species detection were initially generated through the decomposition of FeCl<sub>3</sub> mixed with sodium acetate.<sup>78</sup> High temperature solvents such as ethylene glycol provide multiple functionalities for precursor decomposition. Providing both a solvent phase and chemical species for surface adsorption to improve colloidal stability. Upon mixing of FeCl<sub>3</sub> with sodium acetate in ethylene glycol the solution was heated to 200 °C in a polytetrafluoroethylene (PTFE) lined autoclave vessel for 8 hours. This process is highlighted by the Schikorr reaction and given by eqn (3.4)–(3.6) where upon formation of the FeO-OH and Fe(OH)<sub>2</sub> compounds, thermal energy is used as the driving force to induce decomposition to crystalline magnetite.

## 4. Morphological characterizations

The nanometer regime provides an exceptional opportunity for medical and physical systems innovation but poses a challenge in morphological characterization as the physical limits of optical microscopy become strained near 1 μm when using visible light. Common techniques for the characterization of synthesized nanoparticles include Dynamic Light Scattering (DLS), X-ray Diffraction (XRD), Transmission Electron Microscopy (TEM), Scanning Electron Microscopy (SEM), Energy Dispersive X-ray Analysis (EDX), Raman Spectroscopy, and Fourier Transform Infrared Spectroscopy (FTIR).

### 4.1 Dynamic light scattering

While imaging techniques such as transmission and scanning electron microscopy allow for determination of hard radii and geometrical morphology such as spherical, cylindrical structures, etc., dynamic light scattering provides the important piece of information not gained through TEM/SEM, morphological behavior in a dynamic fluid. The basis behind DLS is derived from the diffraction principle of light as it travels through a medium. Fitting a decay function with respect to the scattering vector ( $q$ ) leads to the obtainment of the diffusion coefficient ( $D$ ), and ultimately to the hydrodynamic radius ( $R_h$ ).<sup>79</sup> The hydrodynamic radius is a dimension which represents a theoretical perfect sphere which would diffuse at a rate equivalent to the suspended particle. In biological appli-

cations it is important to examine the hydrodynamic radii of the constructed nanoparticle as a protein corona quickly forms around the nanoparticle surface in most cases<sup>80,81</sup> effectively increasing particle size over the hard radius observed in TEM/SEM. Fig. 5c displays the characteristic distribution profile of hydrodynamic diameters for a colloidal suspension poly(acrylic acid) (PAA) coated Fe<sub>3</sub>O<sub>4</sub> (PAA/Fe<sub>3</sub>O<sub>4</sub>). Taking the mean hydrodynamic diameter and standard deviation, the polydispersity index (PDI) of hydrodynamic radii can be obtained. A PDI less than 0.1 may be considered to be representative of a narrow size distribution with the PDI calculated as:

$$\text{PDI} = \left( \frac{\sigma}{R_d} \right)^2 \quad (4.1)$$

### 4.2 X-ray diffraction

XRD is a pivotal tool in characterizing the successful synthesis of metal type nanoparticles and nanoparticles with high crystallinity; it relies on the similar principle of constructive interference that is the basis of DLS. Unlike DLS, XRD uses a photon wavelength a few orders of magnitude smaller (CuK $\alpha$  possesses a wavelength of 1.54 Å whereas visible light is on the order of 10<sup>3</sup> Å). As a multitude of crystalline planes exist in any one crystalline structure, the scattering angle is slowly varied across the duration of the experiment. While it may be expected that equal crystalline structures produce diffraction peaks at equal scattering angles, two crystalline materials with different molecular formulas will produce different peak intensities. This is a product of the presence of different scattering lengths possessed by the different elements and even different isotopes of the same element.<sup>82</sup> Examination of peak positions and relative peak intensities allows for identification of synthesized materials. XRD is also applicable to semicrystalline polymers albeit with peak broadening and inclusion of an amorphous halo over a wide range of scattering angles. Fe<sub>3</sub>O<sub>4</sub> possesses an isometric crystal structure belonging to the *Fd3m* space group. Fe<sub>3</sub>O<sub>4</sub> nanoparticle prepared by co-precipitation have a reported lattice parameter near 8.32 Å, which differs from the reported lattice parameter near 8.39 Å for bulk material. This variance has been attributed to the formation of other iron oxide phases during co-precipitation.<sup>83</sup> Tabulation of reflection planes with the respective diffraction angles, relative peak intensities, and interplanar spacing is shown in Table 1.

**Table 1** X-ray diffraction characteristics of Fe<sub>3</sub>O<sub>4</sub>

d-spacing (Å)	$\theta$ (°)	Intensity (relative)	Plane
4.852	18.3	8	111
2.967	30.1	30	220
2.5432	35.3	100	311
2.424	37.1	8	222
2.099	43.1	20	400
1.7146	53.4	10	422
1.6158	56.9	30	511
1.4845	62.5	40	440
1.2807	73.9	10	620
1.093	89.6	12	622

### 4.3 Transmission electron microscopy/scanning electron microscopy/energy dispersive X-ray analysis

TEM provides an exceptional tool for examination of shape and structural morphologies of synthesized nanoparticles through use of an electron beam interacting with sample specimen. An electron beam is generated through the application of a high voltage source, generally a few hundred kV with higher resolutions obtained through a greater electron beam intensity generated by the application of higher voltages, applied to the electron emission source located at the top of the TEM instrument. Fig. 5a depicts multiple nuclei of  $\text{Fe}_3\text{O}_4$  entrapped within a PS matrix while Fig. 5b shows the image of PAA/ $\text{Fe}_3\text{O}_4$ . Hard diameters may be estimated from nanoparticles in the focal plane if the nanoparticles are known to possess a generally spherical geometry.

SEM utilizes similar principles to TEM in the generation and focusing of the electron beam. The electron beam may be scanned across the sample, maintained at a single position, and focused in size. Scintillator and solid state detectors are employed to capture the intensity information of the scattered electrons and the intensity information is then used to generate an intensity map of the topology of the test sample. A convenient secondary analysis to run concurrent with SEM is EDX. During inelastic scattering of electrons from the main beam, an inner shell electron may be ejected. This leaves an electron hole in the inner orbital which is promptly filled by an electron from an outer shell, releasing a photon during the relaxation. As varying elements carry varying numbers of electrons with more populated electronic orbitals as the atomic number increases, characteristic X-ray signatures for specific elements may be identified. With a high signal to noise ratio EDX offers a convenient method to examine atomic species of the surface of nanoparticles such as in the verification of surface conjugation of quantum dots and other species.<sup>22,84–89</sup>

### 4.4 Fourier transform infrared spectroscopy and Raman spectroscopy

The basis of IR spectroscopy lies in the absorption of photons of a specific wavelength which correspond to specific quantized vibrational energy levels with the energy of the photon determined through the classical equation relating photon energy ( $E$ ) to Plank's constant ( $h$ ), the speed of light ( $c$ ), and the photon wavelength ( $\lambda$ ) by the relation,  $E = \frac{hc}{\lambda}$ . As the applied beam passes through the sample only the specific photons of energy ( $E$ ) relating to the signature quantized vibrational bands of their respective and exclusive molecules are absorbed. This allows for examination of surface moieties. As a range of frequency patterns are passing through a sample at any given time for FTIR rather than individual frequencies of the older infrared instruments, a special analysis method is required. Performing a Fourier transform on the measured photonic spectrum output in the time domain ( $f(t)$ ) allows for examination of the attenuation of the transmitted beam in the frequency spectrum ( $F(q)$ ). Fig. 6a shows an attenuated total

reflectance-FTIR spectrograph of silicon dioxide coated nanoparticles referenced against standard silicon dioxide. The characteristic peaks of silicon dioxide appear at 1070, 800, and 445 wavenumbers.

Raman spectroscopy relies on a slightly different mechanism of photonic interaction with a test species. This provides the opportunity to probe spectroscopic signatures which would be absent in IR spectroscopy and may allow for differentiation between samples otherwise difficult to separate by IR spectroscopy. Rather than examine the sample with a range of frequencies and the respective absorbance, Raman spectroscopy employs a main high intensity beam normally in the visible region of only one wavelength and relies on photonic scattering rather than absorption. Shifts in the energy of the photons from the main beam following scattering events are measured. The change in wavenumbers, known as the *Stokes Shift*, is calculated from the inverse of the wavelength of the change in energy. Fig. 6b and c shows the Raman signature of bulk magnetite. The Stokes shifts are displayed using varying main beam intensity and two incident wavelengths. Identification of magnetite is made through the observance of the Stokes shift near  $668 \text{ cm}^{-1}$ . This peak is characteristic of magnetite and is attributed to the  $a_{1g}$  symmetry of the lattice.<sup>90</sup> As can be seen from Fig. 6b and c, increasing laser power causes a phase transformation to hematite from magnetite. This observation has been reported in previous Raman studies.<sup>90</sup>

## 5 Optical properties of iron oxide

### 5.1. Electronic band structure of $\text{Fe}_3\text{O}_4$

Iron oxides in the form of magnetite ( $\text{Fe}_3\text{O}_4$ ), maghemite ( $\text{Fe}_2\text{O}_3$ ), and hematite ( $\text{Fe}_2\text{O}_3$ ) are abundant in nature; they are available in soils, rocks, several species of bacteria, on mars surface,<sup>91</sup> as well as in human body. But the most stable form of iron oxides that are widespread in the environment is magnetite ( $\text{Fe}_3\text{O}_4$ ) and hematite. Over the time, magnetite oxidizes to maghemite and at very high temperature magnetite changes to hematite.<sup>92</sup> The optical properties of hematite were well investigated, and several theoretical and experimental investigations reveal a band gap of 2.1–2.2 eV of hematite that has a potential application in the solar energy conversions.<sup>93,94</sup> Magnetite is also a potential candidate for solar energy conversion due to its light absorption capabilities from visible to near infrared range. But of particular, magnetite in the form of ferrofluid, which consists of very small size nanoparticles, has the applications in magnetic recording, dynamic loudspeakers, as well as in biological applications e.g. in photothermal therapy and in MRI contrast agent.

Magnetite was subject of continuous study in early years, due to its discovery of semiconductor to metal phase transition at 119 K, known as Verway transition temperature.<sup>95</sup> Till then, magnetic and optical properties of this material are subject of continuous interest. Optical investigations of the magnetite were conducted by reflectivity,<sup>96,97</sup> photoelectron, polarization,<sup>98</sup> and magneto-optical spectroscopy techniques.<sup>99,100</sup>

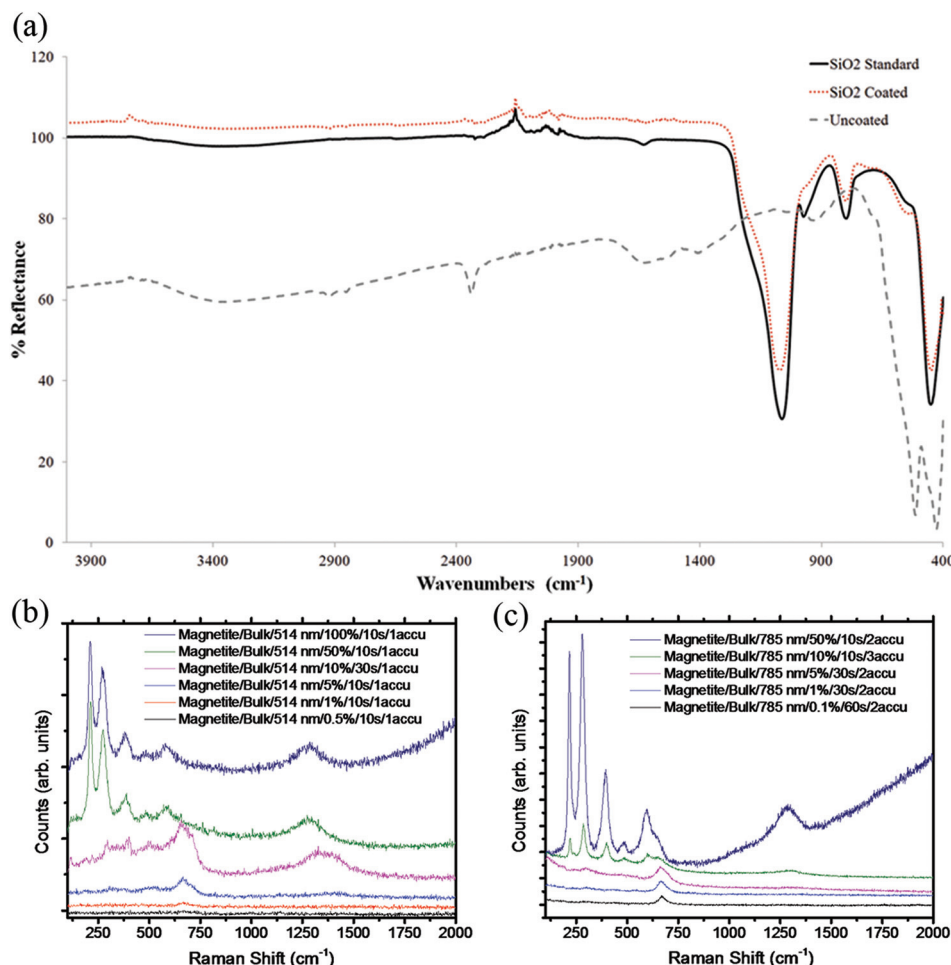


**Fig. 6** (a) Uncoated hematite nanoparticles modified with a silicon dioxide layer. The uncoated nanoparticles appear as dashed grey lines. Characteristic peaks of silicon dioxide are observed for the standard and the surface coating at 1070, 800, and 445 wavenumbers. (b), (c) Raman spectra of bulk magnetite powder using 514, and 785 nm lasers respectively. Peaks are more resolved from the 785 nm measurements and display the characteristic magnetite peak near  $668\text{ cm}^{-1}$  assigned to  $a_{1g}$  symmetry.

Despite of extensive studies, the electronic band structure of  $\text{Fe}_3\text{O}_4$  is still a subject of debate due to a variety of interpretations about assignment of different transitions. This section will therefore, briefly summarize the electronic band structures of  $\text{Fe}_3\text{O}_4$  that are theoretically and experimentally investigated by the researchers over the years.

Bulk magnetite ( $\text{Fe}_3\text{O}_4$ ) has an inverse spinel structure, which consists of face-centered-cubic lattice of  $\text{O}^{2-}$  ions where the tetrahedral (A) site is occupied by  $\text{Fe}^{3+}$  and approximately equal numbers of  $\text{Fe}^{3+}$  and  $\text{Fe}^{2+}$  ions occupy the octahedral (B) site according to the chemical formula  $(\text{Fe}^{3+})[\text{Fe}^{3+}\text{Fe}^{2+}](\text{O}^{2-})_4$ . Several studies have shown that the valence band of the  $\text{O}(2\text{p})$  to the empty  $\text{Fe}(4\text{s})$  in  $\text{Fe}_3\text{O}_4$  is separated by 4–6 eV.<sup>101,102</sup> Between these bands are the crystal field bands of the octahedral and tetrahedral sites that are composed of 3d metal atomic orbital. Several previous experimental measurements and theoretical calculations have reported that the energy gap due to crystal-field splitting on the octahedral site is  $\Delta_{\text{cf}, o} \sim 2.2$  eV, while that of the tetrahedral site is  $\Delta_{\text{cf}, t} \sim 0.9$  eV. The

valence band of  $\text{O}(2\text{p})$  is further separated from crystal field site  $t_{2g}$ ,  $e$  of the octahedral and tetrahedral site respectively by almost  $\sim 0.9$  eV.<sup>94,103</sup> Using photoelectron spin polarization (ESP), energy distribution curve (EDC), ultra and far-ultraviolet photoelectron spectroscopy measurements and with the single ion in crystal field (SICF) model, Alvarado *et al.* have investigated the one electron energy level of  $\text{Fe}_3\text{O}_4$  to describe 3d photoelectronic excitation.<sup>98</sup> Later Balberg *et al.*<sup>104</sup> reported a more comprehensive study of one electron energy level of iron oxide by combining Alvarado's work. The analysis on the reflection and absorption measurements over (0.1–0.5) eV and (0.5–6 eV) were performed by assuming that  $\text{FeO}$ ,  $\text{Fe}_3\text{O}_4$  and  $\text{Fe}_2\text{O}_3$  have the same characteristic spectroscopic signature. An absorption edge at 2 eV and some well resolved peak at 1.5 eV, 3.2 eV and 5.5 eV were identified in their measurements. The absorption edge at 2 eV was assigned to the optical transition of last occupied (d) band to the 4s(Fe) band. Also using the value of  $\Delta_{\text{cf}} = 1.7$  eV due to crystal field splitting, and  $\Delta_{\text{ex}} = 2.7$  eV due to the Hund's rule exchange splitting between the

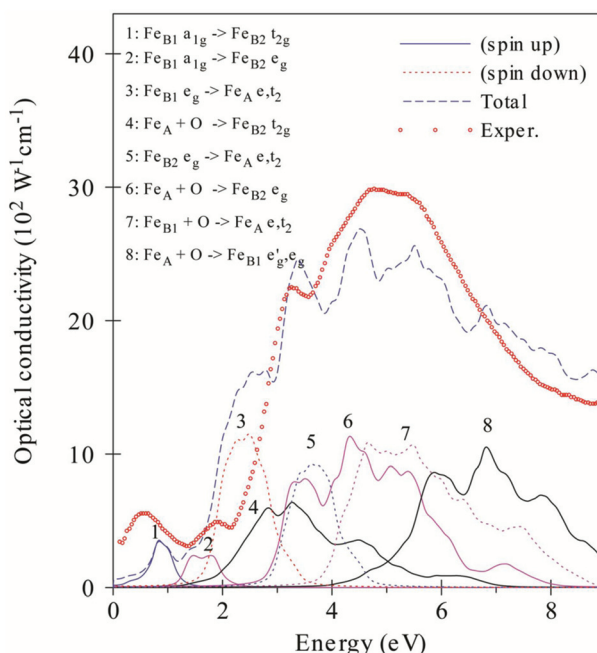


**Fig. 7** Different Interband transitions to the absorptive part of the diagonal optical conductivity of  $\text{Fe}_3\text{O}_4$ .<sup>106</sup> The open circle represents the experimental data collected from Park *et al.*<sup>107</sup> [Fig. 7 is reproduced with permission from American Physical Society © 2001 The American Physical Society. All rights reserved.]

majority spin levels (assumed spin down), from Alvarado's work<sup>98</sup> and combining the results from cathodoluminescence (CL)<sup>105</sup> and soft X-ray study, one electron energy level diagram of octahedral sites of  $\text{Fe}_3\text{O}_4$  was constructed in Fig. 4 of ref. 104.

The electronic structure and magneto-optical Kerr effect of  $\text{Fe}_3\text{O}_4$  was theoretically investigated by Antonov *et al.* using local spin density approximation (LSDA) and LSDA+U approach.<sup>106</sup> Experimental optical and magneto-optical spectra of  $\text{Fe}_3\text{O}_4$  showed a good agreement with the theoretical calculations performed by LSDA+U method. Fig. 7 shows the different interband transitions to the absorptive part of the diagonal optical conductivity of  $\text{Fe}_3\text{O}_4$ . The peaks at 0.9 eV and 2 eV are attributed to the  $\text{Fe}_{\text{B}}^{2+}(\text{a}_{1g}) \rightarrow \text{Fe}_{\text{B}}^{3+}(\text{t}_{2g})$  and  $\text{Fe}_{\text{B}}^{2+}(\text{a}_{1g}) \rightarrow \text{Fe}_{\text{B}}^{3+}(\text{e}_g)$  interband transition, respectively. Peak 3 (2.2 eV) and peak 5 (3.2 eV) are assigned to the transition due to  $\text{Fe}_{\text{B}}^{2+}(\text{e}_g) \rightarrow \text{Fe}_{\text{A}}^{3+}(\text{e}_t)$  and  $\text{Fe}_{\text{B}}^{3+}(\text{e}_g) \rightarrow \text{Fe}_{\text{A}}^{3+}(\text{e}_t)$ , respectively. Peak 4, 6, 7 and 8 are all attributed to the  $\text{O}(2\text{p}) \rightarrow \text{Fe}(3\text{d})$  transitions.<sup>106</sup> These magneto-optical transitions in  $\text{Fe}_3\text{O}_4$  was also observed in the work of Fontijn *et al.*<sup>100,103</sup> and provided the necessary experimental evidence for inter valence charge transfer and intersublattice charge transfer.

## 5.2 Photoexcited properties and charge carrier dynamics in ironoxide

In order for the application of iron oxide nanoparticles in biomedical field as well as for the magneto-optical based devices, understanding is needed on the electronic band structure and charge carrier dynamics. Experimental investigation of band

structure of the iron oxides nanoparticles were reported by a few researchers over the years based on photoluminescence,<sup>108,109</sup> photoelectrophoresis,<sup>93,94</sup> and photocurrent methods.<sup>110,111</sup> Charge carrier dynamics in iron oxide nanoparticles were also studied by time resolved photoluminescence/fluorescence and transient absorption techniques.<sup>112</sup>

Photoluminescence (PL) is not only a phenomenon of light emission from bulk materials, but recently discovered as a characteristic in many nanoparticle systems including quantum dots, silicon, gold, and zinc-blend quantum rods. While PL of these materials involve light emissions from visible to near infrared, the operating excitation mechanisms can range from bound exciton in quantum dots, to surface plasmon in metal nanoparticles. The interband defect states and/or quantum confinement also play important roles in porous nanoparticles of silicon. Photoluminescence measurements of spatially arranged  $\text{Fe}_3\text{O}_4$  particles were studied by Sadat *et al.*<sup>108</sup> over a broad size range of (10 nm–5  $\mu\text{m}$ ). They found three major PL peaks near 560 nm, 695 nm, and 840 nm, when illuminated with 407 nm laser light for all samples [Fig. 8a]. Similar characteristic features were observed in the fluorescence spectra with an excitation wavelength of 350 nm [Fig. 8b]. Fig. 8c and d shows the schematic diagram of the spatial confinement of the  $\text{Fe}_3\text{O}_4$  nanoparticles in the polystyrene matrix ( $\text{PS}/\text{Fe}_3\text{O}_4$ ) and corresponding electronic band structures constructed from PL observations and the proposed model. According to Fig. 8, the PL peak at 565 nm (2.2 eV) is attributed to the radiative recombination of mobile electrons from  $\text{t}_{2g} \rightarrow \text{e}_g$  (2.2 eV) on the octahedral site, and the peak at ~690 nm (1.79 eV) is associated to the recombination of trapped electrons from the octahedral site to  $\text{O}(2\text{p})$ , or  $\text{t}_2 \rightarrow \text{O}(2\text{p})$  on tetrahedral site. The peak at ~840 nm (1.47 eV) is assigned to the transition due to electron traps (created by oxygen vacancies) on the tetrahedral site. In addition to the electronic band structure, a blue shift in the PL peak was also observed due to the quantum confinement effect for the 10 nm diameter  $\text{Fe}_3\text{O}_4$  particles, coated with poly(acrylic acid) (PAA/ $\text{Fe}_3\text{O}_4$ ). Furthermore, much higher PL intensity was observed when the  $\text{Fe}_3\text{O}_4$  nanoparticles are spatially confined in the polystyrene matrix due to collective emissions of light. Photothermal heating measurements performed by 785 nm laser light reveals that PAA/ $\text{Fe}_3\text{O}_4$  has a higher photothermal conversion efficiency (76%) compared to the nanoparticles embedded in the polystyrene matrix ( $\text{PS}/\text{Fe}_3\text{O}_4$ ) (28%). These observations are consistent with the fact that individually coated nanoparticles undergo more non-radiative recombination than the confined system, resulting in much lower PL intensity.

Boxall *et al.*<sup>94</sup> showed that the colloidal  $\text{Fe}_3\text{O}_4$  nanoparticles exhibit three distinct mobility change onset at 1.8, 2.2 and 3.1 eV, which are consistent with the electronic band structure of  $\text{Fe}_3\text{O}_4$ . Based on these three characteristic features of mobility changes, they concluded that  $\text{Fe}_3\text{O}_4$  and  $\text{Fe}_2\text{O}_3$  have almost the identical electronic band structures.

In order to study the charge carrier dynamics of iron oxide nanoparticles, transient absorption measurements were per-

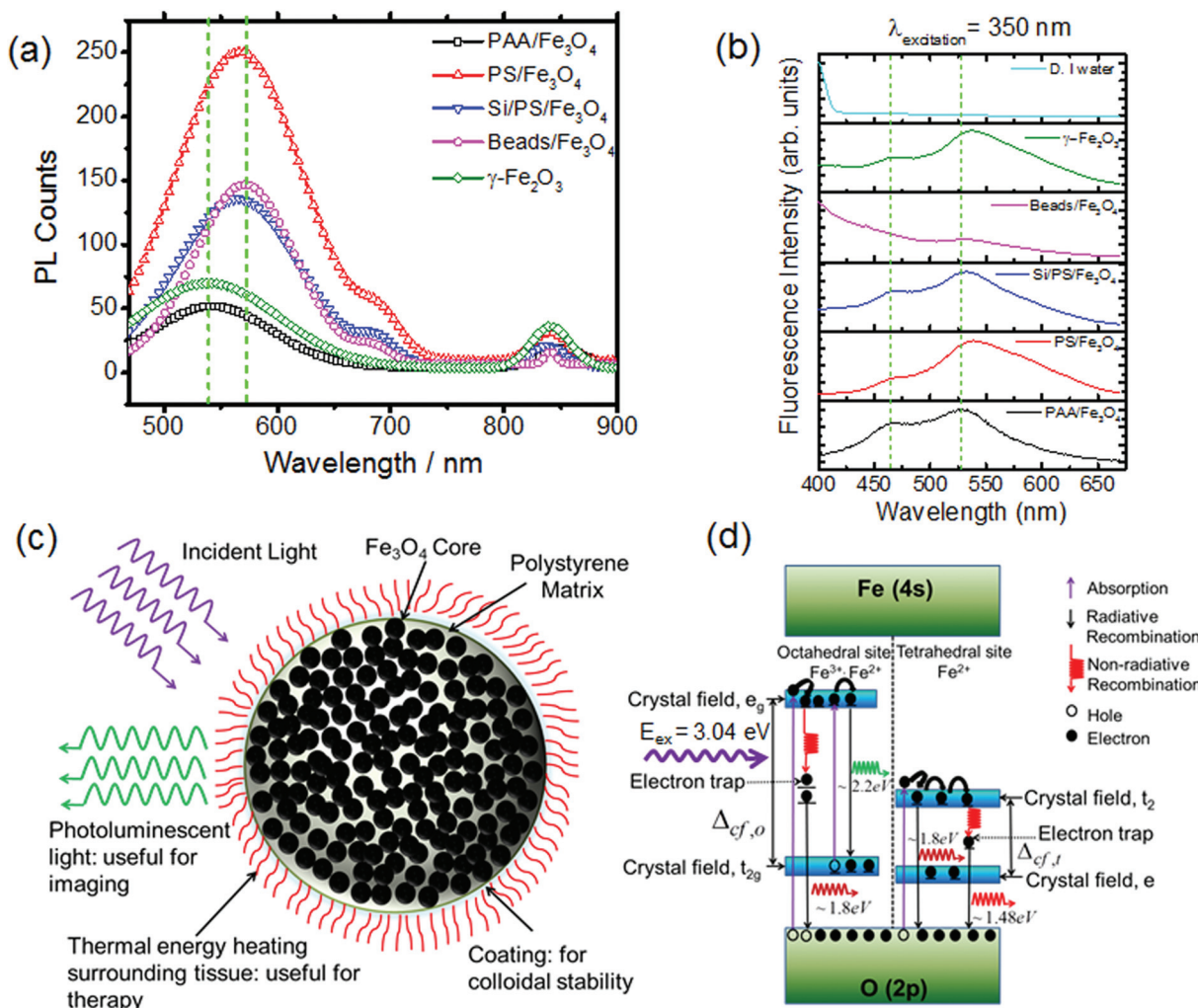


**Fig. 8** (a) The PL spectra of different surface modified iron oxide nanoparticles. The spectra represented in (a) are the cumulative peak fit to the experimental PL data; the vertical dashed lines show the shift in PL peak due to quantum confinement effect.<sup>108</sup> (b) Fluorescence spectra of Fe<sub>3</sub>O<sub>4</sub> nanoparticles as a function emission wavelength. (c) Schematic representation of spatially confined Fe<sub>3</sub>O<sub>4</sub> nanoparticles embedded in a spherical polystyrene matrix, denoted as PS/Fe<sub>3</sub>O<sub>4</sub> and Si/PS/Fe<sub>3</sub>O<sub>4</sub>. (d) Schematic energy bands of the Fe<sub>3</sub>O<sub>4</sub> nanoparticle systems.<sup>108</sup> [Part (a-d) is reproduced with permission from American Institute of Physics (AIP) © 2014 AIP publishing LLC All rights reserved.]

formed by several researchers.<sup>112,113</sup> In their technical approach, nanoparticles were at first excited with femtosecond (fs) or picosecond (ps) short laser pulse, and the excited charge carriers were probed by another pulse laser that was delayed with respect to the excitation laser. Cherepy *et al.*<sup>112</sup> investigated the photoexcited electron dynamics in 1–2 nm γ-Fe<sub>2</sub>O<sub>3</sub>, commercial 50 nm diameter γ-Fe<sub>2</sub>O<sub>3</sub>, and spindle shape (1 × 5) nm α-Fe<sub>2</sub>O<sub>3</sub> nanoparticles. Using 390 nm, 150 fs excitation laser pulse with a 720 nm probe, the transient absorption decay of all these samples can be well fitted with three exponential function with decay times of 0.36, 4.2, and 67 ps respectively. The decay profiles were found to be independent of pump power, probe wavelength, and pH. Due to fast decay of the transient absorption signal, the photoexcited electron relaxation of these nanoparticles can be attributed to the electron-hole recombination mediated by intrinsic mid-bandgap states or trap states created by the internal defects.

The absorption and emission spectra of these nanoparticle systems showed similarities in electronic structure, and the weak emissions from such nanoparticle systems suggest decays to be mostly non-radiative in nature.

The excessive charge carrier recombination in iron oxide nanoparticles makes them not ideal candidates for photoelectrochemical cells even for their good light absorbing properties.<sup>114</sup> But their photothermal effect due to non-radiative recombination can have potential applications in localized cancer therapy.

## 6. Medical applications

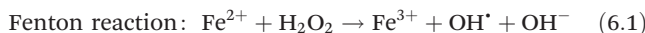
### 6.1 Biocompatibility and toxicity of iron oxide nanoparticles

Iron oxide nanoparticles have shown relatively high toxicity as observed by the medial lethal dose, or the dose required to

induce a 50 percent viability loss in *in vitro* cultures, ( $LD_{50}$ ) and the onset of significant reduction in *in vitro* cellular cultures. *In vivo* biodistribution analysis revealed the most prominent accumulation of untargeted  $Fe_3O_4$  nanoparticles to exist in the liver and spleen, with noted penetration of the blood brain barrier.<sup>115</sup> A multitude of cancerous cell lines have been examined with the general trend of significant onset beginning near  $100\ \mu g\ ml^{-1}$ .<sup>116</sup> Recently the impact of uncoated and coated  $Fe_3O_4$  nanoparticles on *in vitro* MDA-MB-231 human mammary gland adenocarcinoma viability was investigated.<sup>117</sup> Significant reduction in the cellular viability was found to begin at  $25\ \mu g\ ml^{-1}$  with an  $LD_{50}$  of  $1.0 \pm 0.01\ mg\ ml^{-1}$  for the uncoated magnetite. PAA/ $Fe_3O_4$  nanoparticles were found to elicit a drastically reduced toxicity with a significant impact on cellular viability beginning at  $1.0\ mg\ ml^{-1}$  and an  $LD_{50}$  of  $6.3 \pm 0.8\ mg\ ml^{-1}$ .

Coatings, poly(ethylene glycol) specifically, have been known to reduce nanoparticle toxicity and accomplishes this reduction by one of two ways. Cell death *in vitro* may be mediated by two method, chemical and mechanical. Flocculation and sedimentation of unstable colloidal nanoparticle suspensions can cause nanoparticles to coat the cellular surface especially of adherent cells growing on the bottom of culture vessels. This coating may induce death through applied mechanical stresses on the cell membrane or through the blocking of growth factors and required nutrients. Chemical stress may be caused through a range of chemical interactions within the cell. Chemical species which interfere with ATP/GTP production, protein translation, gene transcription, and other necessary growth and respiratory cycles may induce apoptosis or necrosis. For magnetite nanoparticles the main concern is chemical toxicity arising from catalytic production of reactive oxygen species (ROS).<sup>118,119</sup> As the crystalline structure of magnetite possesses two  $Fe^{3+}$  and one  $Fe^{2+}$ , the release of these two oxidation states of iron upon intracellular dissolution of magnetite nanoparticles may initiate catalytic ROS production through the Fenton and Haber-Weiss oxidation/reduction pathways as well as other organic radical forming oxidation/reduction pathways.<sup>120</sup>

#### Haber-Weiss reaction



#### Organic radical formation



Intracellular antioxidative complexes such as superoxide dismutase and glutathione peroxidase naturally scavenge

radical species. However oxidation of important intracellular species becomes likely once an overload occurs from reaching the antioxidant capacity of a cell. If sufficient irreversible damage is caused, the cell may initiate apoptosis and ultimately die. Covalently bonded or surface adsorbed coatings serve to increase colloidal stability over uncoated iron oxides through modification of the charge density distribution around the diffuse layer and assists in reducing the mechanical toxicity due to sedimentation of nanoparticles *in vitro*.<sup>117</sup> Furthermore these coatings may serve to reduce the dissolution rate of the metal oxides. In the case of magnetite nanoparticles this would cause a reduction in intracellular release of  $Fe^{3+}$  and  $Fe^{2+}$  ions which then may be more easily managed by iron sequesters such as ferritin.

## 6.2 Bioconjugation

True multi-functionality of nanoparticle systems may be achieved through surface conjugation and coating. For  $Fe_3O_4$  nanoparticles surface coating plays an important role in providing convenient functional groups for the covalent bonding of targeting, imaging, and therapeutic agents. Nanoparticles and therapeutic drugs may be encapsulated and trapped within micellar structures,<sup>84,121,122</sup> polymeric coatings,<sup>2,16</sup> or ceramics such as silicon dioxide layers and functional groups.<sup>19,70,123</sup> Previously, complex micellar structures entrapping  $Fe_3O_4$  were successfully created through the addition of iron salt precursors to preformed micelles sequestering the chemotherapeutic drug doxorubicin (DOX) which acts as a non-selective disruptor of macromolecule biosynthesis and mitosis.<sup>124</sup> Micellar structures were created by dissolution of a peptide-amphiphile with the triblock co-polymer Pluronic F127 in deionized water with doxorubicin complexed with hydrochloric acid. Following the addition of triethylamine, sonication, and vigorous stirring at  $80\ ^\circ C$ , the formation of complex micelles entrapping DOX was completed.  $Fe_3O_4$  nanoparticles were incorporated and trapped by the micelles through mixing the preformed micelles during the co-precipitation of  $Fe_3O_4$  from  $FeCl_3/FeCl_2$  salts under basic conditions.<sup>122</sup>

Biological conjugation may be easily performed through utilization of zero-length crosslinkers such as 1-ethyl-3-(3-dimethylaminopropyl)carbodiimide hydrochloride (EDC) or dicyclohexylcarbodiimide (DCC) which makes use of carbodiimide chemistry to covalently bond a primary or secondary amine to the alpha carbon of a carboxylate group, forming an amide linkage. It is therefore convenient for the surfaces of coated  $Fe_3O_4$  nanoparticle to be populated with amine or carboxylate groups for convenient crosslinking.<sup>125</sup> This provides the opportunity for an array of biological and non-biological species to be easily conjugated to the nanoparticle surfaces for the establishment of quantum dot, fluorescent dye, antibody, and biotin surface functionalization through careful selection of *N*-hydroxysuccinimide (NHS) coupling agents and its derivatives.<sup>125</sup>

Fig. 9 shows the grayscale fluorescence image from a mouse model used to examine the bioapplication of quantum dot

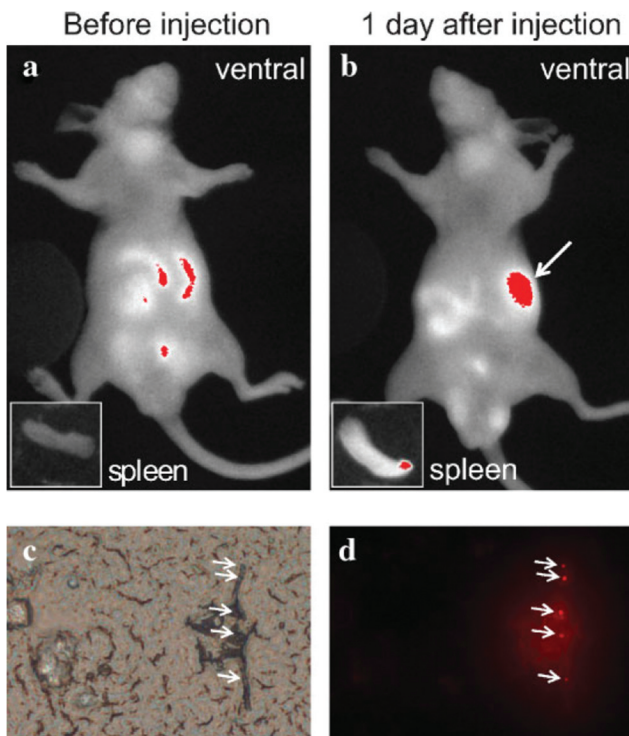


**Fig. 9** *In vivo* and *ex vivo* fluorescent imaging of fluorescently tagged PS/Fe<sub>3</sub>O<sub>4</sub> nanospheres. (a) Auto-fluorescence before intravenous injection. (b) Fluorescence following one day post intravenous injection. Significant increase in spleen fluorescence is observed. (c) Bright-field image of sectioned spleen. (d) Fluorescent image of sectioned spleen shown in (c). Arrows denote prominent accumulation of nanospheres indicated by intense fluorescence.<sup>2</sup> [Fig. 9 is reproduced with permission from WILEY-VCH Verlag GmbH & Co. © 2009 WILEY-VCH Verlag GmbH & Co. All rights reserved.]

labeled nanospheres with Fig. 9a pre-injection and Fig. 9b 24 hours post tail vein injection.<sup>2</sup> Surface functionalization of quantum dots was completed through carbodiimide coupling of an amine functionalized CdSeTe/ZnS core-shell quantum dot to carboxylate groups on the outer shell of the poly(ethylene oxide) PEO coated PS/Fe<sub>3</sub>O<sub>4</sub> nanoparticle using EDC as the zero-length crosslinker. Preferential accumulation of the labeled nanosphere is observed in the spleen, outlined by juxtaposition of the histological spleen cross-section in Fig. 9c along with the respective fluorescent image of the spleen cross section in Fig. 9d. A convenience of the quantum dot is the ability to sheath the quantum dot in a zinc sulfide layer. This not only offers protection to the semi-conductor core but allows for easy conjugation of thiol compounds to the zinc sulfide (ZnS) layer. Upon mixing of a thiol compound with a ZnS layer a co-ordinate (dative) type covalent bond is formed between the sulfur of the thiol and the ZnS layer.<sup>125</sup> Any number of thiol derivatives can be used with terminal carboxylic acid, amine, or NHS functional groups for covalent coupling to conjugated Fe<sub>3</sub>O<sub>4</sub> nanoparticles.

Fig. 10 shows the optical and fluorescent images of targeted and non-targeted Fe<sub>3</sub>O<sub>4</sub> nanoparticles to PC3mm2 and LNCaP

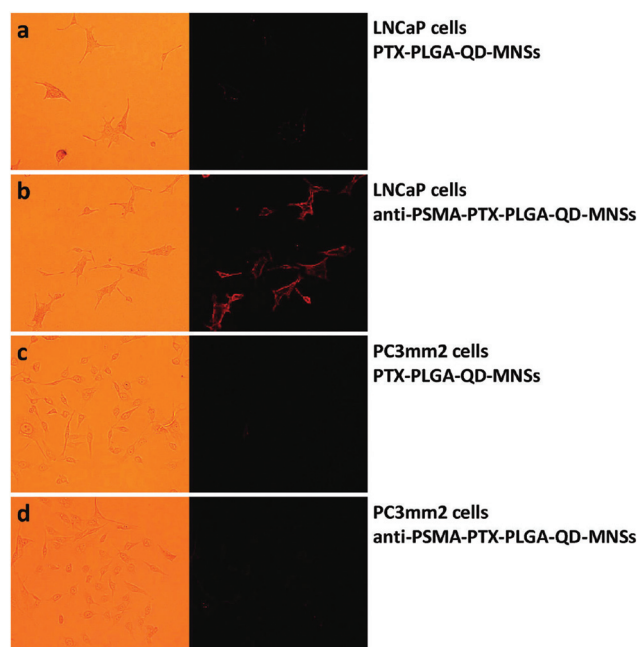


**Fig. 10** *In vitro* fluorescent imaging of prostate cancer lines tagged with fluorescent PS/Fe<sub>3</sub>O<sub>4</sub> nanospheres. (a) Shows LNCaP *in vitro* cells incubated with fluorescent PS/Fe<sub>3</sub>O<sub>4</sub> nanospheres without active targeting. No fluorescence is noted shows no passive targeting of the nanosphere. (b) LNCaP cells successfully targeted *in vitro* through anti-prostate specific membrane antigen antibody. (c) PC3mm2 cells *in vitro* incubated with nanospheres without active targeting. (d) PC3mm2 cells do not possess the prostate specific membrane antigen, thus active targeting has failed. [Fig. 10 is reproduced with permission from ACS Publications © 2010 ACS Publications. All rights reserved.]

human prostate cancer cells. Following the formation of PS/Fe<sub>3</sub>O<sub>4</sub> nanospheres, a O/W emulsion method was employed to coat the nanosphere with carboxy-terminated PLGA along with the mitotic inhibitor paclitaxel (PTX). Quantum dot conjugation was created through an amide linkage of an NHS derivatized CdSeTe/ZnS core-shell quantum dots with the poly(lactic-co-glycolic acid) (PLGA) coated PS/Fe<sub>3</sub>O<sub>4</sub> nanospheres to allow for fluorescent imaging and confirmation of successful cell targeting. To allow for antibody conjugation, ethylenediamine was mixed with the carboxyl terminated PLGA coated PS/Fe<sub>3</sub>O<sub>4</sub> forming an amide bond with one of the primary amines on ethylenediamine; this leave the second primary amine available to participate in covalently linking antibodies to the nanosphere through a second amide bond. Carbodiimide coupling by EDC was subsequently used to functionalize the construct surface with immunoglobulin G (IgG) targeted towards prostate-specific membrane antigen (anti-PSMA) to improve the active targeting capabilities of the fluorescently labeled, drug loaded PS/Fe<sub>3</sub>O<sub>4</sub> construct. As the PC3mm2 prostate cancer variant is not expected to express the prostate-specific membrane antigen, selective targeting through conjugation of anti-PSMA is not expected to enhance targeting and thus enhance fluorescence intensity over the non anti-PSMA conjugated control. This is observed in Fig. 10d. Anti-PSMA

conjugation of PLGA-PS/Fe<sub>3</sub>O<sub>4</sub> nanospheres is observed to successfully increase targeting of LNCaP prostate cancer over the non-targeted controls as shown in Fig. 10a and b as LNCaP expresses PSMA.

### 6.3 Hyperthermia of cancer cells *via* magnetic field application and laser irradiation of magnetite nanoparticles

**6.3.1 Magnetic hyperthermia.** Thermal energy dissipation into the surrounding environment is mediated by relaxation events and dipole-dipole interactions of magnetic domains.<sup>5</sup> Specific absorption rate (SAR) and power loss are the primary quantifications used to describe localized hyperthermia resulting from the application of an alternating magnetic field. SAR may be determined analytically from the integration of the hysteresis loop. However analytical determination of the area of the hysteresis loop is frequently arduous. Contributions from Brownian and Neél Relaxation of the magnetic domains provide a further method of local heating and is a significant contributor to localized hyperthermia upon reaching the superparamagnetic domain for iron oxide nanoparticles as minimal loss in the hysteresis loop is observed.<sup>5</sup> Upon the application of an alternating magnetic field, local hyperthermia was found to be dependent on Neél Relaxation of the magnetic moment and hysteresis loss.<sup>4</sup>

Local environmental heating by surface functionalized Fe<sub>3</sub>O<sub>4</sub> nanoparticles has been previously demonstrated.<sup>2,4,5,11,12,126,127</sup> An alternating 63 kHz magnetic field with an amplitude of 7 kA m<sup>-1</sup> was applied to a 0.1 ml magnetic fluid comprised of 50 mg of the PEO capped PS/Fe<sub>3</sub>O<sub>4</sub> nanoparticles with an average diameter of 100 nm. A temperature rise from 27 °C to 52 °C was observed over a time period of 30 minutes. This was further explored using Fe<sub>3</sub>O<sub>4</sub> nanoparticles with a myriad of coatings including uncoated, Si/PS/Fe<sub>3</sub>O<sub>4</sub>, and PAA/Fe<sub>3</sub>O<sub>4</sub>. Application of 4.5 kA m<sup>-1</sup> magnetic field with a frequency of 13.56 MHz was able to produce a significant change in temperature over the course of the 35 minute application period.

These measured changes in local temperature mediated by magnetic hyperthermia show the possibility in cancer treatment as hyperthermic treatment is known as an effective treatment method.<sup>1</sup> Using Pluronic F-127 encapsulated oleic acid coated Fe<sub>3</sub>O<sub>4</sub> nanoparticles, significant reductions in cellular viability were observed following 60 minutes application of a 16 kA m<sup>-1</sup>, 210 kHz field and at 30 and 60 minutes application of a 20 kA m<sup>-1</sup>, 210 kHz field. Furthermore no deleterious effects were observed when examining the impact of the applied field on the reference HeLa cultures without application of nanoparticles.<sup>128</sup> Magnetic hyperthermia treatments of *in vitro* MBT-2 cultures targets with anti-HER2 antibodies showed similar results with a significant reduction in cellular viability following a 20 minute application of a 1.3 MHz, 33 kA m<sup>-1</sup> magnetic field.<sup>6</sup>

The application of magnetite nanoparticles to be used in therapeutic methods as either the predominant treatment modality or as a sensitizer has been demonstrated through *in vivo* magnetic hyperthermia.<sup>6,7</sup> Drug resistant cell lines can

provide a unique challenge to conventional chemotherapeutics as these cell lines possess the capability to expel chemotherapeutics from the cytosol. This ability has been linked with commonly found molecular pumps, P-glycoprotein and the other multidrug resistance associated protein. As such, this phenotype provides an excellent model to examine the applicability Fe<sub>3</sub>O<sub>4</sub> nanoparticle mediated magnetic hyperthermia. A tumor model was created by establishing a xenograft of K562/A02 multi-drug resistant human leukemia in nude mice. Five treatment groups were comprised of a positive control injected with 0.2 ml of 0.9% saline, daunorubicin (DNR) at 1 mg kg<sup>-1</sup>, 5-bromotetrandrine (5-BrTet) at 1 mg kg<sup>-1</sup> and DNR and 1 mg kg<sup>-1</sup>, Fe<sub>3</sub>O<sub>4</sub> nanoparticles at 22 mg kg<sup>-1</sup>, and Fe<sub>3</sub>O<sub>4</sub>-DNR-5-BrTet loaded nanoparticles at 24 mg kg<sup>-1</sup> in which the DNR and 5-BrTet were at 1 mg kg<sup>-1</sup>. Fe<sub>3</sub>O<sub>4</sub>-DNR-5-BrTet loaded nanoparticles displayed a significantly larger tumor inhibition rate compared to the Fe<sub>3</sub>O<sub>4</sub> treated group. Both nanoparticle injected groups possessed a tumor volume reduction at twelve days compared to the zero day volume, demonstrating the applicability for pure Fe<sub>3</sub>O<sub>4</sub> and Fe<sub>3</sub>O<sub>4</sub> drug loaded nanoparticles in magnetic hyperthermia treatments.<sup>7</sup> In clinical oncology the utility of a intravenous (IV) injection over direct tumor injection provides major benefits such as systemic delivery, allowing for simultaneous deliver of therapeutics without the need for multiple direct injections. A recent study explored the utility of IV injection in treatment of *in vivo* MBT-2 tumors in C3H/HeN mice. Anticancer drug 5-fluorouracil (5-FU) was loaded onto Fe<sub>3</sub>O<sub>4</sub> nanoparticles through polyadenine conjugation. MBT-2 target was achieved through conjugation of anti-human epidermal growth factor receptor 2 (anti-HER2). 200 µl of 500 µg ml<sup>-1</sup> (iron concentration) of Fe<sub>3</sub>O<sub>4</sub>-5-FU-anti-HER2 nanoparticles were injected once every 24 hours with a 15 minute magnetic field application time 24 hours following injection. Fig. 11a shows the measured tumor volume during the study. Significant reduction in tumor volume using the targeted drug loaded nanoparticles against the non-targeted 5-FU (at equal concentration) was achieved, highlighting the importance and clinical applicability of drug loaded, targeted nanoparticles. Furthermore the applicability of magnetic hyperthermia is heavily outlined. Hyperthermia treatment combined with the chemotherapeutic 5-FU induced a near complete reduction in tumor volume while no deleterious effects were observed in systemic regions 48 hours post injection (heart, lung, kidney, liver, spleen).<sup>6</sup>

**6.3.2 Optical hyperthermia.** Optical hyperthermia is a product of the photothermal effect governed by the interaction of electromagnetic (EM) radiation with the magnetite core by absorption and surface plasmon resonance (SPR). For Fe<sub>3</sub>O<sub>4</sub> nanoparticles, the photothermal effect has been observed upon application of EM radiation in the near infrared (NIR) region.<sup>21,129,130</sup> Conveniently this region of the electromagnetic spectrum coincides with a cumulative minimum absorption by water, oxygenated hemoglobin, and deoxygenated hemoglobin.<sup>131</sup> With this combined minimum absorption in biological bodies it is highly pertinent to use nanoparticle composites which elicit a photothermal response when sub-

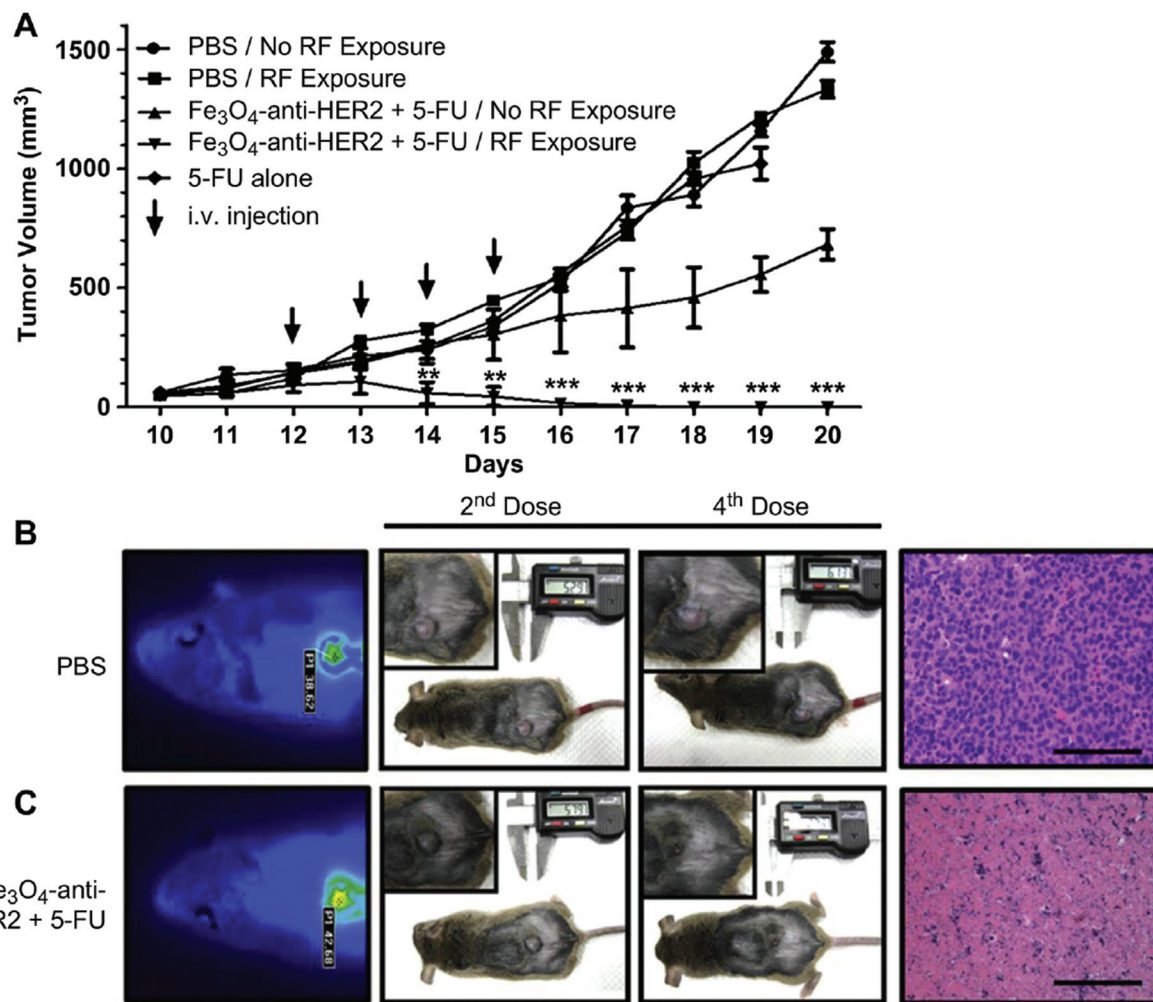


**Fig. 11** (a) Measured *in vivo* volumes from established MBT-2 tumors showing synergy of hyperthermia in conjunction with the antimetabolite 5-fluorouracil delivered by targeted Fe<sub>3</sub>O<sub>4</sub> nanoparticles. (b) PBS alone when injected intravenously did not perturb the tumor state. H&E staining revealed intact tumor cells. (c) Intravenous injection of targeted Fe<sub>3</sub>O<sub>4</sub> nanoparticles with 5-FU and localized hyperthermia mediated tumor remission. H&E staining revealed mass autolysis of MBT-2 cells from the treated area.<sup>6</sup> [Fig. 11 is reproduced with permissions from Elsevier © 2013 Elsevier. All rights reserved].

jected to EM radiation in the NIR region. Fig. 12b depicts temperature profiles of PAA/Fe<sub>3</sub>O<sub>4</sub> nanoparticles, 34 ± 11 nm  $D_h$  in pH 7.4 Hank's Balanced Salt Solution (HBSS) upon irradiation of a 785 nm wavelength laser at an irradiance of 38.5 kW m<sup>-2</sup>. For cellular thermal ablation a general minimum temperature of 42 °C is regarded as being required to bring degradative effects which lead to apoptosis or necrosis.<sup>132</sup> As clinical oncology is concerned with the removal of tumorous lesions without relapse, the time required to successfully thermally ablate cancerous tissue at 42 °C would not be practical if thermal energy alone was used as the treatment modality. It is therefore preferred that a particular setup (utilized nanoparticle construct, nanoparticle concentration, EM wavelength, irradiance, local environment) allows for a plateau temperature of greater than 42 °C or is in conjunction with other treatment modalities such as chemotherapeutics.

Thermal ablation has been highly successful in both *in vitro* and *in vivo*.<sup>21,117</sup> Fig. 12a shows the thermal ablation profile of *in vitro* MDA-MB-231 cultures using PAA/Fe<sub>3</sub>O<sub>4</sub> nanoparticles dispersed in HBSS, irradiated with a 785 nm, 38.5 kW m<sup>-2</sup> NIR laser for 15 minutes referenced against the innate toxicity profiles of uncoated and poly(acrylic acid) coated Fe<sub>3</sub>O<sub>4</sub>. The positive control was established by irradiating MDA-MB-231 cultures with a 785 nm, 38.5 kW m<sup>-2</sup> NIR laser for 15 minutes in the absence of nanoparticles. It can be noted that the significant reduction in *in vitro* viability coincides with the concentration that induces a local temperature rise of greater than 42 °C. The photothermal effect of magnetite nanoparticles has also been investigated utilizing an 808 nm NIR laser in conjunction with *in vitro* human esophageal squamous carcinoma (eca-109). Stable colloidal suspension was established through sonication of magnetite nanoparticle powder with distearoyl-N-[3-carboxypropionoyl

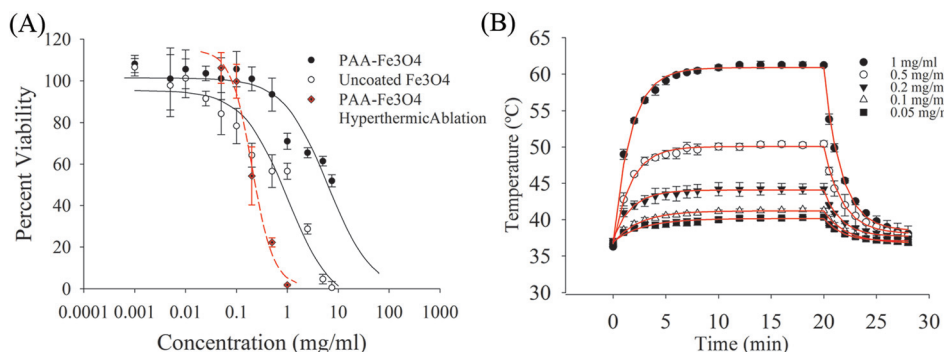


**Fig. 12** (a) *In vitro* innate toxicity of uncoated, PAA coated Fe<sub>3</sub>O<sub>4</sub> compared against *in vitro* thermal ablation using a 37.5 kW m<sup>-2</sup>, 785 nm NIR laser with a 15 minute application time. (b) Time/concentration dependent temperature profile of PAA coated Fe<sub>3</sub>O<sub>4</sub> using a 37.5 kW m<sup>-2</sup>, 785 nm NIR laser.

poly(ethylene glycol) succinyl] phosphatidylethanolamine (DSPE-PEG-COOH). Concentrations of 0.1, 0.5, and 1 mg ml<sup>-1</sup> DSPE-PEG-Fe<sub>3</sub>O<sub>4</sub> were created with RMPI-1640 containing 10% FCS and 1% antibiotics/antimycotics. Cultured wells were subject to 20 minutes of irradiation and referenced against wells containing equal concentrations of nanoparticles not subjected to irradiation. All wells during irradiation were maintained at 37 °C. Viability was measured 60 minutes following irradiation. Significant reduction in viability was observed at 0.1, 0.5, 1.0 mg ml<sup>-1</sup> relative to the wells containing nanoparticles without irradiation.<sup>21</sup>

The efficacy of photodynamic therapy *in vivo* was examined using BALB/c nude mice. Eca-109 cells were injected subcutaneously into the right side of five mice. Following seven days small sections of the tumors were resected and implanted into 60 nude mice. Following 10 days of tumor growth, 30 mice with similar tumor masses were selected for photodynamic therapy. Mice were intratumorally injected with 70 µl of 8.0 mg ml<sup>-1</sup> of DSPE-PEG-Fe<sub>3</sub>O<sub>4</sub> nanoparticles suspended in phosphate buffered saline (PBS) and subjected to 808 nm irradiation for 20 minutes every 24 hours for 24 days. Control groups were created by injection of nanoparticle solutions without irradiation and pure PBS without irradiation. Irradiated mice with injected nanoparticles were observed to possess significantly reduced tumor volumes compared to the blank PBS with observable charred hemorrhagic lesions. Moreover there were no significant differences between the blank PBS and PBS with nanoparticles but without irradiation. Mice not subject to irradiation were further observed to develop significant increases in tumor volume for both the blank PBS and PBS dispersed DSPE-PEG-Fe<sub>3</sub>O<sub>4</sub>.<sup>21</sup> Direct injection of 100 µg suspended in 50 µl PBS into U87 tumor bearing nude mice showed a similar highly significant reduction in tumor volume through an application of a 50 kW m<sup>-2</sup>, 808 nm NIR laser for 30 seconds.<sup>133</sup>

A synergistic effect of chemotherapeutic drug and thermal stress may be achieved through the creation of a multifunctional nanocarrier in which the chemotherapeutic drug is sequestered in the nanocarrier and possesses a temperature

dependent release profile. This may allow lower temperatures, of around 42 °C, to be utilized as the thermal stress combined with targeted release of chemotherapeutic drug induces significant cell death.<sup>21</sup>

#### 6.4 Fe<sub>3</sub>O<sub>4</sub> nanoparticles for imaging

Magnetite nanoparticles in the superparamagnetic domain may serve as MRI contrast agents *in vivo* and *in vitro* due to the high proton magnetic moment alignment, T<sub>1</sub>, T<sub>2</sub> relaxation times, and respective relaxivities<sup>15,16,122,134–136</sup> as well as fluorescent coupling agents for combined multimodal imaging<sup>2,16,17,22,133,134,137–140</sup> A T<sub>2</sub> weighted magnetic resonance intensity plot at varying Fe<sub>3</sub>O<sub>4</sub> concentrations from 10<sup>-15</sup>–10<sup>-1</sup> M juxtaposed against two commercially marketed contrast agents (Magnevist and Resovist) revealed competitive performance. Furthermore, Fe<sub>3</sub>O<sub>4</sub> performed better in serum protein containing solutions than in water.<sup>141</sup> R<sub>1</sub> and R<sub>2</sub> relaxivities of PEG functionalized Fe<sub>3</sub>O<sub>4</sub> nanoparticles created through a one pot synthesis were determined to be 35.92 and 206.91 s<sup>-1</sup> mM<sup>-1</sup> respectively, indicating excellent candidacy for dual contrast MRI.<sup>16</sup> Fig. 13a shows the MRI contrast enhancement achieved through tail vein injection of PEG-Fe<sub>3</sub>O<sub>4</sub> with time-dependent changes in the signal to noise ratio for the liver and spleen shown in Fig. 13b. Significant accumulation of PEG-Fe<sub>3</sub>O<sub>4</sub> was observed in the liver at all time points over other investigated organs, Fig. 13c.

Synergistic enhancement of the magnetic resonance (MR) signal has been observed in formation of gold-magnetite nanorods.<sup>13</sup> This may lead to unique theranostic methods utilizing the MRI properties of magnetite in conjunction with optical and magnetic field induced hyperthermia governed by surface plasmon resonance of gold and dipole interactions of magnetite. Cellular labeling and tracking of endocytosed superparamagnetic iron oxide nanoparticles (SPIONS) coated with poly-L-lysine revealed a rapid intracellular uptake with near intracellular clearance of the of the magnetically active SPION-poly-L-lysine complex within the first week. This corresponded with a significant rise in iron concentration seven days following HeLa cell incubation with SPION constructs

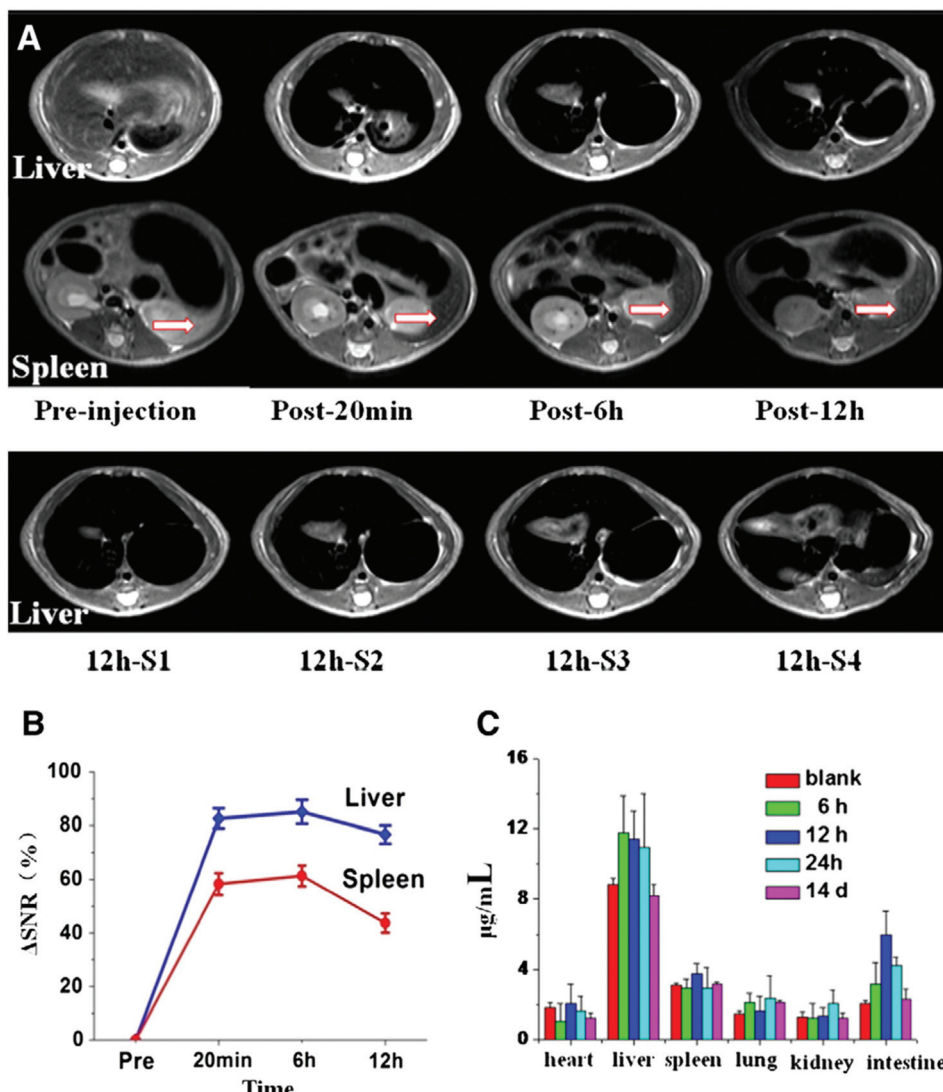


**Fig. 13** (a) MRI of liver and spleen post tail vein injection of PEG- $\text{Fe}_3\text{O}_4$ . (b) Time dependent change in signal to noise ratio of MRI in liver and spleen. (c) Time dependent biodistribution of injected PEG- $\text{Fe}_3\text{O}_4$  showing primary localization in liver.<sup>16</sup> [Fig. 13 is reproduced with permission from Elsevier © 2014 Elsevier. All rights reserved.]

alludes towards release of iron species following intracellular degradation.<sup>142</sup> Release of iron ions into the surrounding environment provides the exciting notion that iron oxide nanoparticles which become decomposed through intracellular processes may be utilized by extracellular iron metabolic pathways such as inclusion into ferritin and hemoglobin. Intravenous injections of SPIONS with inclusion of  $^{59}\text{Fe}$  as a radioactive tracer revealed a 20 percent incorporation of injected iron into hemoglobin 14 days post injection.<sup>143</sup>

PEG conjugated  $\text{Fe}_3\text{O}_4$  loaded bovine serum albumin (BSA- $\text{Fe}_3\text{O}_4$ -PEG) nanoparticles were used to image the biodistribution of intravenously injected nanoparticles following injection through the femoral vein. Prominent accumulation in the spleen and liver was detected through MRI and fluorescent imaging was used to observe pocket accumulations in the left liver lobe.<sup>134</sup> Significant  $T_1$  shortening and an increase

in the fluorescent signal intensity of the BSA- $\text{Fe}_3\text{O}_4$ -PEG nanoparticles was also observed in the grey matter and hippocampus.<sup>134</sup> Intracellular and extracellular tracking of iron oxide nanoparticles may be easily performed through conjugation of quantum dots or other fluorescent molecules through covalent or van der Waals coupling. Fluorescent tracking of fluorescein isothiocyanate coupled  $\text{Fe}_3\text{O}_4$  conjugated multiwall nanotubes revealed a fast sequestration in low pH lysosomes and endosomes.<sup>133</sup> Fluorescent labeled  $\text{Fe}_3\text{O}_4$  nanoclusters were successfully used in low concentration detection of hepatitis B virus from simulated oral mucosal transudate (OMT) samples.<sup>135</sup>

This demonstrates the high applicability of  $\text{Fe}_3\text{O}_4$  nanoparticles to be used as primary MRI agents in imaging and therapeutic procedures for detecting primary secondary tumors. Due to the high  $R_2$  relaxivity and low  $R_2/R_1$  ratio,  $\text{Fe}_3\text{O}_4$  nano-

particles are not needed to act as the primary delivery vehicle for therapeutics. They may be conjugated to non-magnetically responsive, such as biologically derived (proteins, RNA, etc.), nanoparticles to assist in tracking accumulation and biodistribution from intravenous delivery. Moreover the magnetic and optical hyperthermic responses can be easily applied to directly injected or passive/active targeted tumor sites to establish  $\text{Fe}_3\text{O}_4$  nanoparticles as truly theranostic in nature.

## 7. Present status and future developments of clinical study

Clinical applications of hyperthermic treatments have yielded promising results in solid tumor treatment. Applicability in clinical settings of solid tumors is depended upon the exotic vascularization morphology observed. Tortuous weaves of disseminated, underdeveloped blood vessels in solid tumors create perfused areas with poor waste management. In normal tissue, normal vascularization will act as a heat sink reducing the temperature of local hyperthermic regions. Herein lies the difference; solid tumor vasculature provides a poor heat sink. Current hyperthermia techniques in late stage clinical trials and practice include: ultrasound, radio waves (100 kHz–150 MHz), microwaves (433–2450 MHz), hot water perfusions and boluses, resistive wire implant, and ferromagnetic materials.<sup>1</sup> Recent early and late stage clinical trials have further proven the applicability of hyperthermic treatments in combination with chemotherapeutics,<sup>144,145</sup> small molecules,<sup>146</sup> and as the sole agent.<sup>147</sup> Primarily hyperthermia is currently used as an adjuvant therapy to reduce treatment time and accelerate tumor regression. However with the high multimodal functionality of  $\text{Fe}_3\text{O}_4$  nanoparticles and the ability to deliver targeted chemotherapeutics, primary treatment methods utilizing  $\text{Fe}_3\text{O}_4$  based nanoparticles show great promise for innovative therapies.

## 8. Conclusions

Considering the iron oxide nanoparticles a non-interacting system, we have analyzed its magnet behavior in AC magnetic using the Langevin model. For a variety of iron oxide particles with different sizes, distributions, and physical confinements, we have reviewed their magnetic hyperthermia with several heating mechanisms, namely, Néel and Brownian relaxations, and hysteresis loss, based on the most recent experimental and theoretical studies in the literature. Also reported is the photo luminescence of iron oxide nanoparticles in a wide frequency range from visible to NIR. The emission behaviors are well explained based on the electronic band structures of the iron oxides.

Magnetite nanoparticles have been shown to possess multimodal functionality with applications in imaging diagnostics and therapeutic treatments and are easily synthesized through an array of methods. Common methods include co-precipi-

tation of dissolved iron salts with a basic solution and decomposition of iron acetylacetone allowing for monodisperse, tunable sizes. Single and double emulsion methods can be used to coat  $\text{Fe}_3\text{O}_4$  nanoparticles with polymeric species for drug loading and conjugation targeting, imaging, or therapeutic moieties. With magnetic relaxivities allowing for  $T_1$  or  $T_2$  weighted imaging, multi-modal imaging can be achieved through the innate magnetic properties in combination with conjugated fluorescent species. This offers exciting possibilities for image assisted diagnosis and resection of tumor masses with magnetic resonance offering deep tissue imaging prior to resection and fluorescent imaging during resection to assist in the obtainment of a clean edge. Furthermore, local, targeted hyperthermia of solid tumors using  $\text{Fe}_3\text{O}_4$  nanoparticles has already shown success *in vivo*. Such multi-modal functionality, with local heating achieved from applied alternating magnetic fields or near infrared radiation and imaging achieved through conjugation of fluorescent species and magnetic resonance imaging, establishes the versatility and applicability of  $\text{Fe}_3\text{O}_4$  nanoparticles in clinical use.

## Acknowledgements

The authors would like to thank the National Science Foundation for research funding through award number EEC-1343568, Dr Giovanni Pauletti of the College of Pharmacy, University of Cincinnati for their invaluable research assistance. We would like to thank Dr Rodney Ewing's group of the Department of Geological & Environmental Sciences, Stanford University for providing our TEM images, and Dr Hong Xu of the School of Biomedical Engineering, Med-X Research Institute, Shanghai Jiao Tong University for synthesis of the PAA/ $\text{Fe}_3\text{O}_4$  and PS/ $\text{Fe}_3\text{O}_4$  nanoparticles.

## References

- 1 A. Chicheł, J. Skowronek, M. Kubaszewska and M. Kanikowski, *Rep. Pract. Oncol. Radiother.*, 2007, **12**, 267–275.
- 2 D. Shi, H. S. Cho, Y. Chen, H. Xu, H. Gu, J. Lian, W. Wang, G. Liu, C. Huth, L. Wang, R. C. Ewing, S. Budko, G. M. Pauletti and Z. Dong, *Adv. Mater.*, 2009, **21**, 2170–2173.
- 3 F. Wang, G. M. Pauletti, J. Wang, J. Zhang, R. C. Ewing, Y. Wang and D. Shi, *Adv. Mater.*, 2013, **25**, 3485–3489.
- 4 M. E. Sadat, R. Patel, J. Sookoor, S. L. Bud'ko, R. C. Ewing, J. Zhang, H. Xu, Y. Wang, G. M. Pauletti, D. B. Mast and D. Shi, *Mater. Sci. Eng., C*, 2014, **42**, 52–63.
- 5 M. E. Sadat, R. Patel, S. L. Bud'ko, R. C. Ewing, J. Zhang, H. Xue, D. B. Mast and D. Shi, *Mater. Lett.*, 2014, **129**, 57–60.
- 6 T. Li, C. Huang, P. Ruan, K. Chuang, K. Huang, D. Shieh and C. Yeh, *Biomaterials*, 2013, **34**, 7873–7883.

- 7 Y. Ren, H. Zhang, B. Chen, J. Cheng, X. Cai, R. Liu, G. Xia, W. Wu, S. Wang, J. Ding, C. Gao, J. Wang, W. Bao, L. Wang, L. Tian, H. Song and X. Wang, *Int. J. Nanomed.*, 2012, **7**, 2261–2269.
- 8 S. Sun and H. Zeng, *J. Am. Chem. Soc.*, 2002, **124**, 8204–8205.
- 9 D. Dunlop, *J. Geophys. Res.*, 1973, **78**, 1780–1793.
- 10 J. Li, Y. Qu, J. Ren, W. Yuan and D. Shi, *Nanotechnology*, 2012, **23**, 505706.
- 11 T. Kobayashi, *Biotechnol. J.*, 2011, **6**, 1342–1347.
- 12 R. Hergt, W. Andra, C. d'Ambly, I. Hilger, W. Kaiser, U. Richter and H. Schmidt, *IEEE Trans. Magn.*, 1998, **34**, 3745–3754.
- 13 C. Wang, J. Chen, T. Talavage and J. Irudayaraj, *Angew. Chem., Int. Ed.*, 2009, **121**, 2797–2801.
- 14 F. Xu, C. Cheng, D. Chen and H. Gu, *ChemPhysChem*, 2012, **13**, 336–341.
- 15 F. Hu, Q. Jia, Y. Li and M. Gao, *Nanotechnology*, 2011, **22**, 245604.
- 16 L. Dai, Y. Liu, Z. Wang, F. Guo, D. Shi and B. Zhang, *Mater. Sci. Eng., C*, 2014, **41**, 161–167.
- 17 H. Cho, Z. Dong, G. M. Pauletti, J. Zhang, H. Xu, H. Gu, L. Wang, R. C. Ewing, C. Huth, F. Wang and D. Shi, *ACS Nano*, 2010, **4**, 5398–5404.
- 18 E. Song, J. Hu, C. Wen, Z. Tian, X. Yu, Z. Zhang, Y. Shi and D. Pang, *ACS Nano*, 2011, **5**, 761–770.
- 19 G. Zhang, Y. Liao and I. Baker, *Mater. Sci. Eng., C*, 2010, **30**, 92–97.
- 20 A. M. Schrand, B. M. Stacy, S. Payne, L. Dosser and S. M. Hussain, *ACS Appl. Mater. Interfaces*, 2011, **3**, 3971–3980.
- 21 M. Chu, Y. Shao, J. Peng, X. Dai, H. Li, Q. Wu and D. Shi, *Biomaterials*, 2013, **34**, 4078–4088.
- 22 D. Shi, N. M. Bedford and H. Cho, *Small*, 2011, **7**, 2549–2567.
- 23 J. Carrey, B. Mehdaoui and M. Respaud, *J. Appl. Phys.*, 2011, **109**, 083921.
- 24 F. Heider, D. J. Dunlop and N. Sugiura, *Science*, 1987, **236**, 1287–1290.
- 25 R. Hergt, R. Hiergeist, M. Zeisberger, G. Glöckl, W. Weitschies, L. Ramirez, I. Hilger and W. Kaiser, *J. Magn. Magn. Mater.*, 2004, **280**, 358–368.
- 26 R. Hergt, S. Dutz and M. Röder, *J. Phys.: Condens. Matter*, 2008, **20**, 385214.
- 27 E. C. Stoner and E. Wohlfarth, *Philos. Trans. R. Soc. London, Ser. A*, 1948, **240**, 599–642.
- 28 M. Shliomis, *Phys. -Usp.*, 1974, **17**, 153.
- 29 L. Néel, *Adv. Phys.*, 1955, **4**, 191–243.
- 30 R. E. Rosensweig, *J. Magn. Magn. Mater.*, 2002, **252**, 370–374.
- 31 G. Vallejo-Fernandez, O. Whear, A. Roca, S. Hussain, J. Timmis, V. Patel and K. O'Grady, *J. Phys. D: Appl. Phys.*, 2013, **46**, 312001.
- 32 P. Fannin, *J. Magn. Magn. Mater.*, 2003, **258**, 446–451.
- 33 P. C. Fannin, B. Scaife and S. Charles, *J. Magn. Magn. Mater.*, 1988, **72**, 95–108.
- 34 M. Hanson, *J. Magn. Magn. Mater.*, 1991, **96**, 105–113.
- 35 D. Chen, A. Sanchez, H. Xu, H. Gu and D. Shi, *J. Appl. Phys.*, 2008, **104**, 093902.
- 36 G. Bellizzi, O. Bucci and A. Capozzoli, *J. Magn. Magn. Mater.*, 2010, **322**, 3004–3013.
- 37 N. Song, H. Yang, H. Liu, X. Ren, H. Ding, X. Zhang and Z. Cheng, *Sci. Reports*, 2013, **3**, 3161.
- 38 P. Fannin, S. Charles and T. Relihan, *J. Magn. Magn. Mater.*, 1997, **167**, 274–280.
- 39 S. Lin, D. Yun, D. Qi, C. Deng, Y. Li and X. Zhang, *J. Proteome Res.*, 2008, **7**, 1297–1307.
- 40 U. I. Tromsdorf, O. T. Bruns, S. C. Salmen, U. Beisiegel and H. Weller, *Nano Lett.*, 2009, **9**, 4434–4440.
- 41 M. Respaud, *J. Appl. Phys.*, 1999, **86**, 556–561.
- 42 J. Dormann, D. Fiorani and E. Tronc, *Adv. Chem. Phys.*, 1997, **98**, 283–494.
- 43 J. Fortin, C. Wilhelm, J. Servais, C. Ménager, J. Bacri and F. Gazeau, *J. Am. Chem. Soc.*, 2007, **129**, 2628–2635.
- 44 M. Gonzales-Weimuller, M. Zeisberger and K. M. Krishnan, *J. Magn. Magn. Mater.*, 2009, **321**, 1947–1950.
- 45 K. Bakogiannis, K. Simeonidis, D. Sakellari, G. Stefanou and M. Angelakeris, *Magnetics, IEEE Transactions on*, 2012, **48**, 1320–1323.
- 46 P. Hugounenq, M. Levy, D. Alloyeau, L. Lartigue, E. Dubois, V. Cabuil, C. Ricolleau, S. Roux, C. Wilhelm and F. Gazeau, *J. Phys. Chem. C*, 2012, **116**, 15702–15712.
- 47 A. Walter, C. Billotey, A. Garofalo, C. Ulhaq-Bouillet, C. Lefèvre, J. Taleb, S. Laurent, L. Vander Elst, R. N. Muller and L. Lartigue, *Chem. Mater.*, 2014, **26**, 5252–5264.
- 48 J. Fortin, F. Gazeau and C. Wilhelm, *Eur. Biophys. J.*, 2008, **37**, 223–228.
- 49 R. Hergt, R. Hiergeist, I. Hilger, W. Kaiser, Y. Lapatnikov, S. Margel and U. Richter, *J. Magn. Magn. Mater.*, 2004, **270**, 345–357.
- 50 G. Vallejo-Fernandez and K. O'Grady, *Appl. Phys. Lett.*, 2013, **103**, 142417.
- 51 L. C. Branquinho, M. S. Carrião, A. S. Costa, N. Zufelato, M. H. Sousa, R. Miotto, R. Ivkov and A. F. Bakuzis, *Sci. Reports*, 2013, **3**, 2887.
- 52 O. Lunov, V. Zablotskii, T. Syrovets, C. Röcker, K. Tron, G. U. Nienhaus and T. Simmet, *Biomaterials*, 2011, **32**, 547–555.
- 53 A. Urtizberea, E. Natividad, A. Arizaga, M. Castro and A. Mediano, *J. Phys. Chem. C*, 2010, **114**, 4916–4922.
- 54 J. Dormann, L. Bessais and D. Fiorani, *J. Phys. C: Solid State Phys.*, 1988, **21**, 2015.
- 55 M. F. Hansen and S. Mørup, *J. Magn. Magn. Mater.*, 1998, **184**, L262–L274.
- 56 P. Jönsson, J. García-Palacios, M. F. Hansen and P. Nordblad, *J. Mol. Liq.*, 2004, **114**, 131–135.
- 57 D. Berkov and N. Gorn, *J. Phys.: Condens. Matter*, 2001, **13**, 9369.
- 58 C. Martinez-Boubeta, K. Simeonidis, A. Makridis, M. Angelakeris, O. Iglesias, P. Guardia, A. Cabot, L. Yedra, S. Estradé, F. Peiró, Z. Saghi, P. A. Midgley, I. Conde-

- Leborán, D. Serantes and D. Baldomir, *Sci. Reports*, 2013, **3**, 1652.
- 59 Y. Piñeiro-Redondo, M. Bañobre-López, I. Pardiñas-Blanco, G. Goya, M. A. López-Quintela and J. Rivas, *Nanoscale Res. Lett.*, 2011, **6**, 1–7.
- 60 C. Haase and U. Nowak, *Phys. Rev. B: Condens. Matter*, 2012, **85**, 045435.
- 61 D. Serantes, D. Baldomir, C. Martínez-Boubeta, K. Simeonidis, M. Angelakeris, E. Natividad, M. Castro, A. Mediano, D. Chen and A. Sanchez, *J. Appl. Phys.*, 2010, **108**, 073918.
- 62 J. Vargas, W. Nunes, L. Socolovsky, M. Knobel and D. Zanchet, *Phys. Rev. B: Condens. Matter*, 2005, **72**, 184428.
- 63 J. García-Otero, M. Porto, J. Rivas and A. Bunde, *Phys. Rev. Lett.*, 2000, **84**, 167.
- 64 U. Nowak, *Annu. Rev. Comput. Phys. IX*, 2001, **9**, 105–151.
- 65 V. Singh and V. Banerjee, *J. Appl. Phys.*, 2012, **112**, 114912.
- 66 S. Gudoshnikov, B. Y. Liubimov and N. Usov, *AIP Adv.*, 2012, **2**, 012143.
- 67 J. Fortin, C. Wilhelm, J. Servais, C. Ménager, J. Bacri and F. Gazeau, *J. Am. Chem. Soc.*, 2007, **129**, 2628–2635.
- 68 L. Castro, M. Da Silva, A. Bakuzis and R. Miotto, *J. Magn. Magn. Mater.*, 2005, **293**, 553–558.
- 69 S. Dutz and R. Hergt, *Nanotechnology*, 2014, **25**, 452001.
- 70 S. Wang, J. Tang, H. Zhao, J. Wan and K. Chen, *J. Colloid Interface Sci.*, 2014, **432**, 43–46.
- 71 S. Laurent, D. Forge, M. Port, A. Roch, C. Robic, L. Vander Elst and R. N. Muller, *Chem. Rev.*, 2008, **108**, 2064–2110.
- 72 M. Ma, Y. Zhang, Z. Guo and N. Gu, *Nanoscale Res. Lett.*, 2013, **8**, 1–7.
- 73 N. Mizutani, T. Iwasaki, S. Watano, T. Yanagida, H. Tanaka and T. Kawai, *Bull. Mater. Sci.*, 2008, **31**, 713–717.
- 74 A. P. A. Faiyas, E. M. Vinod, J. Joseph, R. Ganesan and R. K. Pandey, *J. Magn. Magn. Mater.*, 2010, **322**, 400–404.
- 75 H. Xu, L. Cui, N. Tong and H. Gu, *J. Am. Chem. Soc.*, 2006, **128**, 15582–15583.
- 76 S. M. Joscelyne and G. Trägårdh, *J. Membr. Sci.*, 2000, **169**, 107–117.
- 77 Q. Lan, C. Liu, F. Yang, S. Liu, J. Xu and D. Sun, *J. Colloid Interface Sci.*, 2007, **310**, 260–269.
- 78 Y. Tang, S. Liang, S. Yu, N. Gao, J. Zhang, H. Guo and Y. Wang, *Colloids Surf. A*, 2012, **406**, 61–67.
- 79 B. J. Berne and R. Pecora, *Dynamic light scattering: with applications to chemistry, biology, and physics*, Courier Dover Publications, 2000.
- 80 C. Gunawan, M. Lim, C. P. Marquis and R. Amal, *J. Mater. Chem. B*, 2014, **2**, 2060–2083.
- 81 A. E. Nel, L. Mädler, D. Velegol, T. Xia, E. M. Hoek, P. Somasundaran, F. Klaessig, V. Castranova and M. Thompson, *Nat. Mater.*, 2009, **8**, 543–557.
- 82 R. Roe and R. Roe, *Methods of X-ray and neutron scattering in polymer science*, Oxford University Press, New York, 2000.
- 83 H. El Ghandoor, H. Zidan, M. M. Khalil and M. Ismail, *Int. J. Electrochem. Sci.*, 2012, **7**, 5734–5745.
- 84 M. Chu, H. Li, Q. Wu, F. Wo and D. Shi, *Biomaterials*, 2014, **35**, 8357–8373.
- 85 J. Li, L. Zu, Y. Li, C. Jin, Y. Qin, D. Shi and J. Yang, *J. Colloid Interface Sci.*, 2014, **426**, 90–98.
- 86 Y. Guo, D. Shi, J. Lian, Z. Dong, W. Wang, H. Cho, G. Liu, L. Wang and R. C. Ewing, *Nanotechnology*, 2008, **19**, 175102.
- 87 Y. Guo, D. Shi, H. Cho, Z. Dong, A. Kulkarni, G. M. Pauletti, W. Wang, J. Lian, W. Liu, L. Ren, Q. Zhang, G. Liu, C. Huth, L. Wang and R. C. Ewing, *Adv. Funct. Mater.*, 2008, **18**, 2489–2497.
- 88 D. Shi, Y. Guo, Z. Dong, J. Lian, W. Wang, G. Liu, L. Wang and R. C. Ewing, *Adv. Mater.*, 2007, **19**, 4033–4037.
- 89 W. Wang, D. Shi, J. Lian, Y. Guo, G. Liu, L. Wang and R. C. Ewing, *Appl. Phys. Lett.*, 2006, **89**, 183106.
- 90 O. N. Shebanova and P. Lazor, *J. Solid State Chem.*, 2003, **174**, 424–430.
- 91 R. M. Cornell and U. Schwertmann, *The iron oxides: structure, properties, reactions, occurrences and uses*, John Wiley & Sons, 2006.
- 92 J. Tang, M. Myers, K. A. Bosnick and L. E. Brus, *J. Phys. Chem. B*, 2003, **107**, 7501–7506.
- 93 Z. Zhang, C. Boxall and G. Kelsall, *Colloids Surf. A*, 1993, **73**, 145–163.
- 94 C. Boxall, G. Kelsall and Z. Zhang, *J. Chem. Soc., Faraday Trans.*, 1996, **92**, 791–802.
- 95 E. Verwey, P. Haayman and F. Romeijn, *J. Chem. Phys.*, 1947, **15**, 181–187.
- 96 A. Schlegel, S. Alvarado and P. Wachter, *J. Phys. C: Solid State Phys.*, 1979, **12**, 1157.
- 97 A. Schlegel and P. Wachter, *Le J. de Phys. Colloq.*, 1980, **41**, C5-19–C5-21.
- 98 S. Alvarado, M. Erbudak and P. Munz, *Physica B*, 1977, **86**, 1188–1190.
- 99 X. Zhang, J. Schoenes, W. Reim and P. Wachter, *J. Phys. C: Solid State Phys.*, 1983, **16**, 6055.
- 100 W. Fontijn, P. Van der Zaag, M. Devillers, V. Brabers and R. Metselaar, *Phys. Rev. B: Condens. Matter*, 1997, **56**, 5432.
- 101 J. Zaanen, G. Sawatzky and J. Allen, *Phys. Rev. Lett.*, 1985, **55**, 418.
- 102 D. L. Camphausen, J. M. D. Coey and B. K. Chakraverty, *Phys. Rev. Lett.*, 1972, **29**, 657–660.
- 103 W. Fontijn, P. Van Der Zaag, L. Feiner, R. Metselaar and M. Devillers, *J. Appl. Phys.*, 1999, **85**, 5100–5105.
- 104 I. Balberg and H. Pinch, *J. Magn. Magn. Mater.*, 1978, **7**, 12–15.
- 105 I. Balberg and J. Pankove, *Phys. Rev. Lett.*, 1971, **27**, 1371.
- 106 V. Antonov, B. Harmon, V. Antropov, A. Y. Perlov and A. Yaresko, *Phys. Rev. B: Condens. Matter*, 2001, **64**, 134410.
- 107 S. Park, T. Ishikawa and Y. Tokura, *Phys. Rev. B: Condens. Matter*, 1998, **58**, 3717.
- 108 M. E. Sadat, M. K. Baghbador, A. W. Dunn, H. P. Wagner, R. C. Ewing, J. Zhang, H. Xu, G. M. Pauletti, D. B. Mast and D. Shi, *Appl. Phys. Lett.*, 2014, **105**, 091903.

- 109 J. B. West and H. Broida, *J. Chem. Phys.*, 1975, **62**, 2566–2574.
- 110 J. K. Leland and A. J. Bard, *J. Phys. Chem.*, 1987, **91**, 5076–5083.
- 111 K. Gurunathan and P. Maruthamuthu, *Int. J. Hydrogen Energy*, 1995, **20**, 287–295.
- 112 N. J. Cherepy, D. B. Liston, J. A. Lovejoy, H. Deng and J. Z. Zhang, *J. Phys. Chem. B*, 1998, **102**, 770–776.
- 113 S. R. Pendlebury, X. Wang, F. Le Formal, M. Cornuz, A. Kafizas, S. D. Tilley, M. Graitzel and J. R. Durrant, *J. Am. Chem. Soc.*, 2014, **136**, 9854–9857.
- 114 S. Cai, D. Jiang, R. Tong, S. Jin, J. Zhang and A. Fujishima, *Electrochim. Acta*, 1991, **36**, 1585–1590.
- 115 J. Wang, Y. Chen, B. Chen, J. Ding, G. Xia, C. Gao, J. Cheng, N. Jin, Y. Zhou, X. Li, M. Tang and X. M. Wang, *Int. J. Nanomed.*, 2010, **5**, 861–866.
- 116 B. Ankamwar, T. Lai, J. Huang, R. Liu, M. Hsiao, C. Chen and Y. Hwu, *Nanotechnology*, 2010, **21**, 075102.
- 117 A. W. Dunn, S. M. Ehsan, D. Mast, G. M. Pauletti, H. Xu, J. Zhang, R. C. Ewing and D. Shi, *Mater. Sci. Eng., C*, 2015, **46**, 97–102.
- 118 Y. Hou, M. Lai, X. Chen, J. Li, Y. Hu, Z. Luo, X. Ding and K. Cai, *J. Biomed. Mater. Res., Part A*, 2014, **102**, 1726–1736.
- 119 P. Ma, Q. Luo, J. Chen, Y. Gan, J. Du, S. Ding, Z. Xi and X. Yang, *Int. J. Nanomed.*, 2012, **7**, 4809–4818.
- 120 G. Papanikolaou and K. Pantopoulos, *Toxicol. Appl. Pharmacol.*, 2005, **202**, 199–211.
- 121 H. Wen, H. Dong, W. Xie, Y. Li, K. Wang, G. M. Pauletti and D. Shi, *Chem. Commun.*, 2011, **47**, 3550–3552.
- 122 Y. Li, J. Ma, H. Zhu, X. Gao, H. Dong and D. Shi, *ACS Appl. Mater. Interfaces*, 2013, **5**, 7227–7235.
- 123 M. E. Khosroshahi and L. Ghazanfari, *Physica E*, 2010, **42**, 1824–1829.
- 124 O. Tacar, P. Sriamornsak and C. R. Dass, *J. Pharm. Pharmacol.*, 2013, **65**, 157–170.
- 125 G. T. Hermanson, *Bioconjugate techniques*, Academic press, 2013.
- 126 S. M. Cassim, A. J. Giustini, I. Baker and P. J. Hoopes, *Energy-Based Treatment of Tissue and Assessment Vi*, 2011, **7901**, 790115.
- 127 A. Ito, M. Shinkai, H. Honda and T. Kobayashi, *J. Biosci. Bioeng.*, 2005, **100**, 1–11.
- 128 A. Tomitaka, T. Yamada and Y. Takemura, *J. Nanomater.*, 2012, 480626.
- 129 G. Liu, J. Ma and J. Liu, *J. Shanghai Jiaotong Univ.*, 2012, **17**, 730.
- 130 Q. Tian, J. Hu, Y. Zhu, R. Zou, Z. Chen, S. Yang, R. Li, Q. Su, Y. Han and X. Liu, *J. Am. Chem. Soc.*, 2013, **135**, 8571–8577.
- 131 R. Weissleder, *Nat. Biotechnol.*, 2001, **19**, 316–316.
- 132 S. A. Sapareto and W. C. Dewey, *Int. J. Radiat. Oncol., Biol., Phys.*, 1984, **10**, 787–800.
- 133 S. Shen, J. Ren, X. Zhu, Z. Pang, X. Lu, C. Deng, R. Zhang and X. Jiang, *J. Mater. Chem. B*, 2013, **1**, 1939–1946.
- 134 N. P. M. Vera, R. Schmidt, K. Langer, I. Zlatev, R. Wronski, E. Auer, D. Havas, M. Windisch, H. von Briesen, S. Wagner, J. Stab, M. Deutsch, C. Pietrzik, F. Fazekas and S. Ropele, *PLoS One*, 2014, **9**, e92068.
- 135 H. Hu, H. Yang, D. Li, K. Wang, J. Ruan, X. Zhang, J. Chen, C. Bao, J. Ji, D. Shi and D. Cui, *Analyst*, 2011, **136**, 679–683.
- 136 D. Shi, *Adv. Funct. Mater.*, 2009, **19**, 3356–3373.
- 137 L. Wang, K. Neoh, E. Kang, B. Shuter and S. Wang, *Biomaterials*, 2010, **31**, 3502–3511.
- 138 D. Bhattacharya, S. P. Chakraborty, A. Pramanik, A. Bakshi, S. Roy, T. K. Maiti, S. K. Ghosh and P. Pramanik, *J. Mater. Chem.*, 2011, **21**, 17273–17282.
- 139 J. Wang, Y. Liu, Y. Hou, Z. Chen and N. Gu, *Methods Mol. Biol.*, 2012, **906**, 221–237.
- 140 Y. Hou, Y. Liu, Z. Chen, N. Gu and J. Wang, *J. Nanobiotechnol.*, 2010, **8**, 25.
- 141 F. Cheng, C. Su, Y. Yang, C. Yeh, C. Tsai, C. Wu, M. Wu and D. Shieh, *Biomaterials*, 2005, **26**, 729–738.
- 142 A. Arbab, L. Bashaw, B. Miller, E. Jordan, B. Lewis, H. Kalish and J. Frank, *Radiology*, 2003, **229**, 838–846.
- 143 R. Weissleder, D. D. Stark, B. L. Engelstad, B. R. Bacon, C. C. Compton, D. L. White, P. Jacobs and J. Lewis, *Am. J. Roentgenol.*, 1989, **152**, 167–173.
- 144 B. A. Inman, P. R. Stauffer, O. A. Craciunescu, P. F. Maccarini, M. W. Dewhurst and Z. Vujaskovic, *Int. J. Hyperthermia*, 2014, **30**, 171–175.
- 145 D. Hompes, A. D'Hoore, E. Van Cutsem, S. Fieuws, W. Ceelen, M. Peeters, K. Van der Speeten, C. Bertrand, H. Legendre and J. Kerger, *Ann. Surg. Oncol.*, 2012, **19**, 2186–2194.
- 146 G. Gadaleta-Caldarola, S. Infusino, I. Galise, G. Ranieri, G. Vinciarelli, V. Fazio, R. Divella, A. Daniele, G. Filippelli and C. D. Gadaleta, *Oncol. Lett.*, 2014, **8**, 1783–1787.
- 147 M. Johannsen, U. Gneveckow, L. Eckelt, A. Feussner, N. Waldöfner, R. Scholz, S. Deger, P. Wust, S. Loening and A. Jordan, *Int. J. Hyperthermia*, 2005, **21**, 637–647.